

A change-point random partition model for large spatio-temporal datasets

Andrea Cremaschi, Annalisa Cadonna, Alessandra Guglielmi, Fernando Quintana

Abstract

Spatio-temporal areal data can be seen as a collection of time series which are spatially correlated, according to a specific neighboring structure. Motivated by a dataset on mobile phone usage in the Metropolitan area of Milan, Italy, we propose a semi-parametric hierarchical Bayesian model allowing for time-varying as well as spatial model-based clustering. To accommodate for changing patterns over work hours and weekdays/weekends, we incorporate a temporal change-point component that allows the specification of different hierarchical structures across time points. The model features a random partition prior that incorporates the desired spatial features that encourages co-clustering based on areal proximity. We explore properties of the model by way of extensive simulation studies from which we collect valuable information. Finally, we discuss the application to the motivating data, where the main goal is to spatially cluster population patterns of mobile phone usage.

1 Introduction

In recent years, there has been a rapid increase in the availability of data collected over time on areal units. Areal units can be defined by geographical boundaries (e.g., regions, counties, municipalities), or by tessellating the territory of interest. The available data are often large-to-huge collections of (possibly long) time series that are spatially correlated, according to

a specific neighborhood structure. Data of this type are extremely helpful to understand population distribution in an urban space, which is critical for urban planning and provision of municipal services; see, e.g. Deville et al. [2014], Sulis et al. [2018], and Tu et al. [2020]. However, traditional methods for exploring human population dynamics, such as censuses and surveys, can be very expensive. Moreover, more detailed changes over time, such as daily commute and urban transportation, are challenging to assess with traditional methods, but crucial nonetheless, to urban planning.

Mobile phone-based data have been extensively used to extract geographical knowledge in previous studies; see, for instance, Song et al. [2010] and Liu et al. [2015]. Previous studies on the urban analysis [see Wang et al., 2021, and the references therein] suggest that mobile phone data are a valid proxy for human activities and interactions.

This manuscript uses area-level mobile phone data to represent intra-urban population distribution. Motivated by the study of population density dynamics arising in the context of mobile data, we specify an appropriate model and develop efficient algorithms for the statistical analysis of large-to-huge spatio-temporal areal data. The proposed hierarchical model takes into account various characteristics of the data, including (a) varying regimes corresponding to day/night and workday/weekend times; and (b) time evolving responses recorded throughout a number of days. We also aim at performing time-varying spatial clustering of time series.

The motivating dataset has been previously considered in Manfredini et al. [2015] and Secchi et al. [2015], modeling each time series as the realization of a functional data process. One of the main goals of this work is to model the population dynamics and in particular how this changes across different regimes, and thus our approach does not employ a functional data perspective but rather builds on a combination of harmonic regression models for the temporal component and conditionally autoregressive (CAR) models for the spatial association. CAR models are commonly used to represent spatial autocorrelation for areal data, and can be thought of as the conditional specification of a (Gaussian) Markov random field

(GMRF). A comprehensive review of GMRF models can be found in Rue and Held [2005]. CAR models were originally introduced as spatial models in Besag [1974, 1975], and they have been used since as the likelihood for the observations themselves in one-stage models, or as the distribution of spatial random effects, as part of a Bayesian hierarchical model [see Besag et al., 1991]. The different CAR models proposed in the literature correspond to specific choices of the precision matrix for the corresponding GMRF. Thanks to the Markov property, the precision matrix of a GMRF is potentially very sparse, which enables efficient computation through linear algebra algorithms for sparse matrices. An efficient algorithm for block updating for Markov Random Fields models is introduced in Knorr-Held and Rue [2002]. Different CAR prior specifications have been proposed, such as the intrinsic and Besag-York-Mollié priors [both in Besag et al., 1991]. We adopt instead the formulation proposed in Leroux et al. [2000], which is useful to estimate spatial correlation among the random effects.

Two research domains where areal clustering is important are disease mapping (i.e., disease clustering) and crime studies. For the former, Wehrhahn et al. [2020] propose a Bayesian nonparametric prior, called the Restricted Chinese Restaurant Process, that constrains clusters to be made of adjacent areal units. They apply the model to oral cancer mortality in administrative districts in Germany. Other works on Bayesian methods for disease clustering in spatially aggregated data include, for instance, Knorr-Held and Raßer [2000], Wakefield and Kim [2013] and Anderson et al. [2014]. See also Wehrhahn et al. [2020] for further references. Statistical analyses of crime data can be found in Law et al. [2014] and Li et al. [2014], who assume Bayesian spatio-temporal models to analyse local patterns of crime rates change over time at the small-area level. Balocchi et al. [2021] introduce a Bayesian non-parametric model for the clustering of urban areal units for estimating and clustering crime incidence at various levels of resolution in Philadelphia, US.

The current literature on spatial clustering does not include the partition of areal units in the random parameters of the model, but obtain cluster estimates through application of

empirical clustering methods (e.g. hierarchical clustering) to posterior summaries obtained from the data. Instead, we model the partition of areas directly and make this a central object of posterior inference. Our prior, here denoted areal product partition model (aPPM), penalizes excessive areal disconnectedness through a spatial association parameter ξ .

Finally, a different Bayesian nonparametric model for clustering has been proposed in Cadonna et al. [2019] using the same dataset analysed in this work. There are two main differences between their model and the one proposed in this work. First, in Cadonna et al. [2019], areal units are clustered together if their behaviour is similar over the entire time series under analysis, while we allow for clustering changes across regimes. Second, Cadonna et al. [2019] use an ANOVA-DDP prior which does not consider the neighboring structure of the areal units, while the aPPM introduced in Section 3.2 explicitly takes this into account.

Our contributions to the analysis of spatio-temporal areal datasets can be summarized as follows: (i) we propose a novel spatio-temporal random partition model that has connections with random probability measures of discrete type often found in Bayesian nonparametrics and that provide a satisfactory fit to the available data; (ii) inference on change-points, i.e. the detection of time points where the dynamics of mobile phone usage transits between different regimes; (iii) estimate spatially-driven clusters of areal regions, and assess their changes over regimes; (iv) finally, the proposed approach can naturally handle the fraction of missing responses contained in the data. Our model is specifically designed for the application we consider, i.e. the change over time of the random partitions of the areal units is governed by regimes, thus reducing the number of random partitions under consideration. However, clustering of spatially correlated data, possibly including time-varying clustering, is a lively research area in Bayesian nonparametrics. For instance, Page and Quintana [2016] is the first paper to propose a prior for the random partition of geo-referenced data that models the grouping of locations into spatially dependent clusters, encouraging observations in locations that are close to be put in the same cluster. Page et al. [2022] combine this type of prior with a time-varying clustering context, with applications to geo-referenced data.

The remainder of this paper is organized as follows. Section 2 presents the data and describes the main motivations of this work. Section 3 introduces modeling framework and describes the novel aPPM prior. The results of the application to population density dynamics in the city of Milan are presented in Section 4. Section 5 concludes the paper. Computational details on the MCMC algorithm can be found in Appendix A. An extensive simulation study is carried out in Appendix B. Appendix B reports a performance comparison between the proposed model and some of its variants, as well as competitor models available in the literature, and Appendix B presents some additional plots.

2 Description of the Dataset and Motivation

Motivated by the study of population density dynamics in the metropolitan area of Milan, Italy, we propose a model for spatio-temporal clustering of areal data. We consider data as in Secchi et al. [2015] (more details are reported below), though to understand clustering of areas in the inner part of the city, we focus on a smaller grid. The municipality of Milan, located in the metropolitan area center, is a major productivity and financial center for the entire northern portion of Italy. Indeed, about 1.3 million people live and 600 thousand people commute every working day between Milan and the metropolitan area. Using mobile phone data, we study how the dynamics of the population density evolves over time, potentially uncovering temporal and spatial patterns. Moreover, we would like to partition the areas covered by the data into subregions sharing a similar population dynamic pattern across the observed time window. This is of great interest to urban planners, city managers and network providers. For instance, the data in Secchi et al. [2015] is also analyzed in Manfredini et al. [2015], who investigated relevant urban usage by proposing diversified management policies for increased efficiency of public services supply. Wang et al. [2021] propose a Bayesian spatio-temporal model focusing on area-level mobile phone users data. Specifically, their data are the total number of mobile phone users actively recorded by cell towers in one-hour intervals in an overall time window of 24 hours in Shenzhen, China. They do not assume

a random partition, and infer the clustering structure of the spatial data via a hierarchical clustering procedure on the estimated time profiles. They nevertheless conclude that their Bayesian spatio-temporal model can enhance the understanding of the space-time variability of population distribution using mobile phone data.

The dataset we consider is provided by Telecom Italia, the largest mobile company in Italy, as part of the Green Move Initiative (financed by Regione Lombardia), through a research agreement between Telecom and Politecnico di Milano. See further details in Secchi et al. [2015]. These authors segment the metropolitan area of Milan into subregions that share the same activity pattern along time in terms of population density dynamics. To this end, they integrate a Treelet analysis for dimensional reduction with a Bagging Voronoi strategy for the exploration of spatial dependence, in order to reduce the dimension of spatially dependent signals. They propose the Bagging Voronoi Treelet algorithm, that decompose the massive dataset (10,573 areas for 1,308 time points, resulting in more than 13 millions records) into relevant spatial and temporal dynamics.

In this work, we focus on a portion of the metropolitan area of Milan between 45.44407° and 45.49222° North in latitude and between 9.15° and 9.225° East in longitude. This portion covers approximately the area inside a city belt called *circonvallazione* (i.e., circumvallation), hosting a significant flow of private and public transportation vehicles during rush hours. The districts inside this belt line can be considered the city center. We have partitioned the central area into a grid of $I = 13 \times 14$ sites (areal units).

Each areal unit was recovered from the original data by Telecom, putting together 4 of the original sites from a uniform lattice of an area including the metropolitan area though we consider only inner areal units as stated above. See Figure 1 presenting the portion of the central municipality of Milan under study. The data are recorded every 15 minutes from March 18th 2009, 00:15 to March 31st 2009, 23:45, yielding a time series of length $T = 1343$ for each of the lattice sites. In total, 244,608 records are available of which 22,068 are missing. We analyze the Erlang number, calculated as the sum of lengths of

all calls in a given time interval, divided by the length of the interval. In other words, the Erlang number is equivalent to the average number of mobile phones simultaneously calling through the network, and can be considered proportional to the number of active users [see Secchi et al., 2015, for more details]. The Erlang number, recorded over all areal units in a region, can be used as a proxy for population density in that region, and through its changes over times, of population density dynamics.

Figure 1 shows the standardized log-Erlang number recorded on Wednesday, March 18th 2009 at noon, for the selected portion of the metropolitan area. The financial district in the center of the city is identifiable, as it is the area with high mobile activities during working hours, as well as the eastern area corresponding to a busy portion of the city. We can also identify, for example, peripheral areas with less mobile traffic in the western part. Locations on the grid corresponding to missing observations are left blank, showing only the underlying map of the city. In what follows we always report summary statistics or plots of globally standardized log-Erlang numbers.

Figure 2 shows the time series for 10 randomly selected locations. As we can see, the mobile activity is higher during the day hours and lower at night. Moreover, we can see differences between workdays and weekends. We consider these temporal patterns in the proposed model in such a way that the clustering structure changes over time through a simplified approach based on the notion of temporal regimes (workdays and weekends, days and nights). Another distinguished feature of our Bayesian model is that we can handle missing responses in a natural fashion [unlike, for instance Secchi et al., 2015].

3 Model specification

We now introduce the spatio-temporal hierarchical model for the motivating dataset, which has three main components, namely: (1) the likelihood part for (standardized) log-Erlang numbers, based on a mixed regression with time-varying coefficients and spatially-correlated random effects; (2) the random partition prior specification for areal units, which incorpo-

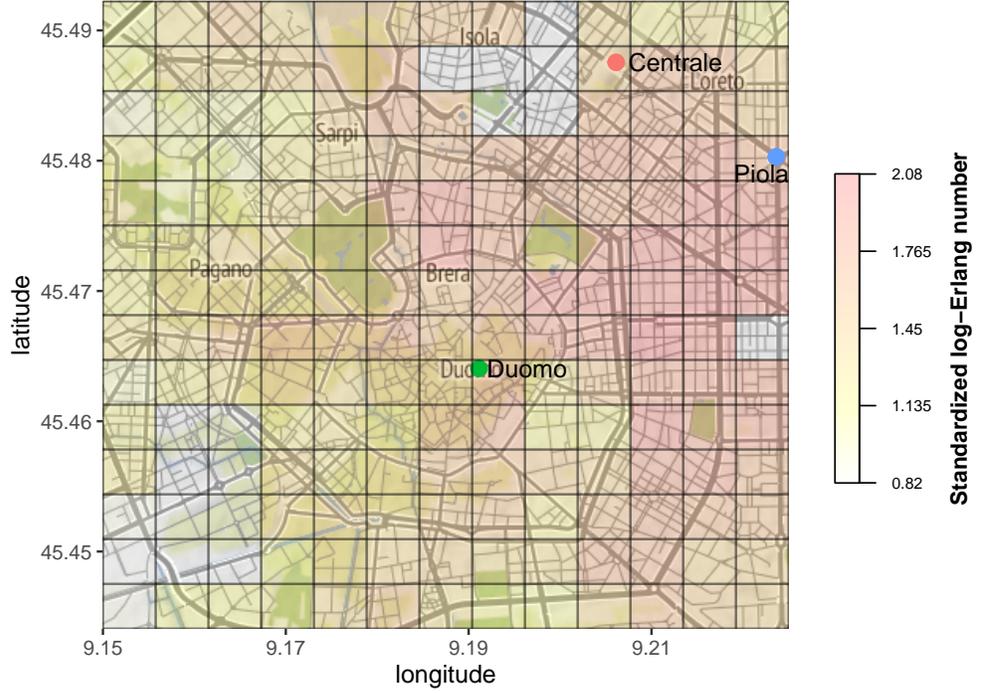


Figure 1: Data recorded on Wednesday March 18th 2009, at noon. The grey areas corresponds to missing observations. Points of interests as Piazza Duomo, Stazione Centrale and Piazza Piola are denoted as colored points. Data shown are standardized log-Erlang numbers for all areal units.

rates information on the spatial structure; and (3) the prior specification for regimes and change-points.

3.1 Likelihood and spatial random effects

Consider I areal units, in our case given by tessellations of part of the city of Milan, as described in Section 2. Denote by Y_{it} the observation for areal unit $i = 1, \dots, I$ at time $t = 1, \dots, T$, yielding a dataset of $I \times T$ observations. In our application, the response variable is the standardized logarithm of the Erlang number. To avoid null Erlang numbers, before applying the logarithmic transformation to the data, we transform them by adding a quantity equal to the smallest observed non-zero Erlang number. It is important to remark

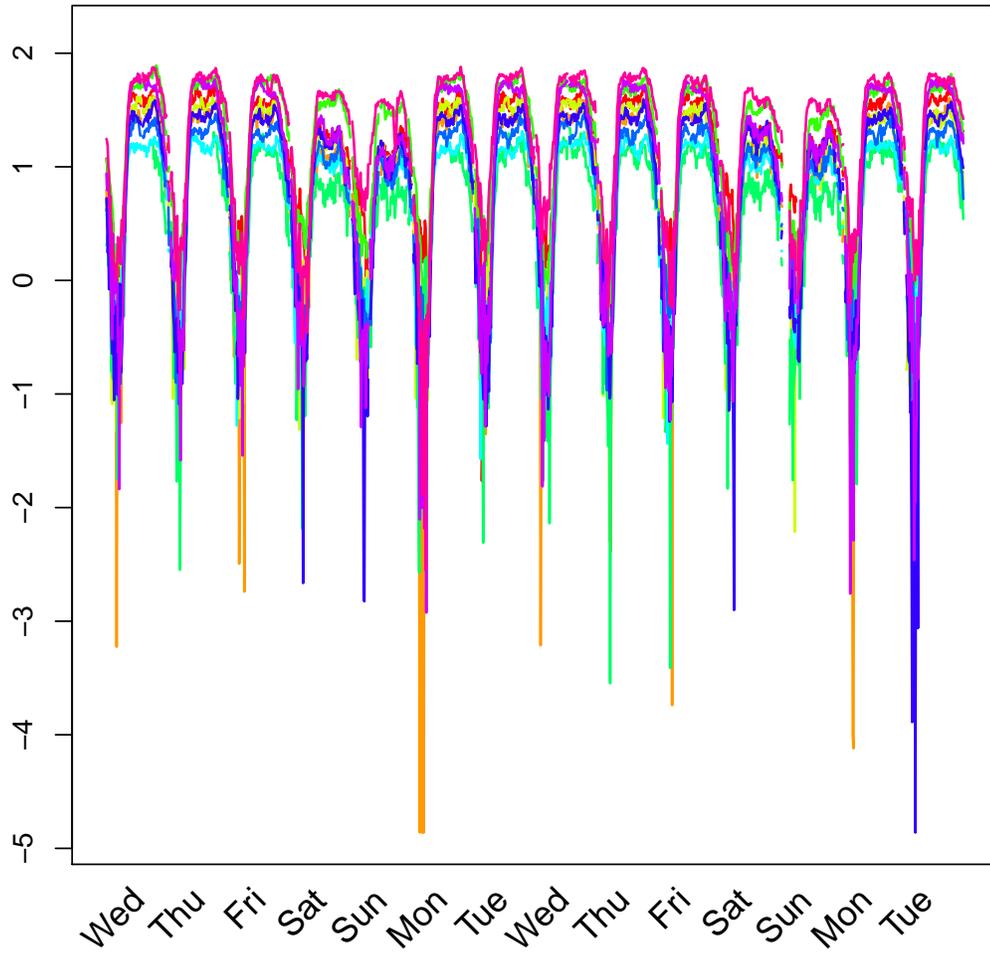


Figure 2: Standardized log-Erlang numbers for data recorded over time at 10 randomly selected locations.

that a zero Erlang number does not mean zero activity, but that this fell below a certain detection threshold. Then, the log-transformed data are standardized to have mean 0 and standard deviation 1.

For each areal unit $i = 1, \dots, I$, and time $t = 1, \dots, T$, we model observation Y_{it} as:

$$Y_{it} \mid \mathbf{x}_t, \tilde{\boldsymbol{\beta}}_{it}, \tilde{u}_{it} = \mathbf{x}'_t \tilde{\boldsymbol{\beta}}_{it} + \tilde{u}_{it} + \epsilon_{it}, \quad \epsilon_{it} \stackrel{\text{ind}}{\sim} \mathbf{N}(0, \sigma_{\epsilon_t}^2) \quad (1)$$

where ϵ_{it} , for $i = 1, \dots, I$ and $t = 1, \dots, T$, are conditionally independent spatio-temporal residuals. See below for the definition of the zero-mean \tilde{u}_{it} . Here, $\mathbf{N}(\mu, \sigma^2)$ denotes the Gaussian distribution with mean μ and variance σ^2 . The p -dimensional extension of it will be used later and indicated as $\mathbf{N}_p(\boldsymbol{\mu}, \boldsymbol{\Sigma})$ for mean vector $\boldsymbol{\mu}$ and covariance matrix $\boldsymbol{\Sigma}$. The variance of ϵ_{it} in the full Bayesian model will depend on the regime associated to t . The mean surface in this model is given by $\mathbf{x}'_t \tilde{\boldsymbol{\beta}}_{it}$, through which we model, at each location, the periodicity of the data by resorting to a harmonic regression. Concretely, we let \mathbf{x}_t denote a K -dimensional design vector, chosen from the harmonic functions $(\cos(\omega_j t), \sin(\omega_j t))$, where $\omega_j = 2\pi j/T$ and $j = 1, 2, \dots, T/2$. If T is not an even number, we assume T to be the next even number and the corresponding observation to be missing. See Appendix A for details on Bayesian imputation of the missing Erlang numbers. In this dataset, since we have 1343 time measurements, we assume $T = 1344$. Note that $T = 1344 = 2 \times 7 \times 24 \times 4$, since our time span is two weeks with four observations per hour. Since our responses are standardized, we exclude the intercept term in \mathbf{x}_t . Using harmonic regression corresponds to approximating each underlying signal through a trigonometric polynomial. Motivated by the characteristics of our dataset and pragmatic knowledge of Milan vehicle traffic, we choose to select weekly, daily, semi-daily and hourly frequencies in \mathbf{x}_t . This is equivalent to assuming $K = 8$, and

$$\mathbf{x}_t = (\cos(\omega_2 t), \sin(\omega_2 t), \cos(\omega_{14} t), \sin(\omega_{14} t), \cos(\omega_{28} t), \sin(\omega_{28} t), \cos(\omega_{336} t), \sin(\omega_{336} t)). \quad (2)$$

For instance, to set the daily frequency, we assume $j = \frac{1344}{24 \times 4} = 14$, so that $\omega_{14} = \frac{2\pi}{96}$. In this case $\cos(\omega_{14}(t + 96)) = \cos(\omega_{14} t)$, i.e. the function has period equal to 96, which corresponds to one day interval (4 observations in an hour for 24 hours). The vector $\tilde{\boldsymbol{\beta}}_{it} = (\tilde{\beta}_{it,1}, \dots, \tilde{\beta}_{it,K})'$ is the vector of harmonic coefficients and, as discussed later in Section 3.3, will be used to cluster the areal units.

Having controlled seasonality through \mathbf{x}_t in our model, we now consider spatial autocorrelation. This is done via a spatial random effects vector $\tilde{\mathbf{u}}_t = (\tilde{u}_{1t}, \dots, \tilde{u}_{It})'$ on which we put a spatial CAR prior, that is:

$$\tilde{\mathbf{u}}_t \mid \tau^2, Q(\zeta_t, W), \zeta_t \sim \mathbf{N}_I(\mathbf{0}, \tau^2 Q(\tilde{\zeta}_t, W)^{-1}) \quad (3)$$

where W is the $I \times I$ matrix encoding the contiguity structure of the I areal units specified as $W_{i,j} = 1$ if areal units i and j are neighbors and $W_{i,j} = 0$ otherwise. Here, we specifically define the neighbors of a site i as the 8 cells surrounding i in a grid layout. To help the description of W , we list its minor diagonals from the main diagonal to the bottom left corner. The only minor diagonals with elements different from zero are the first, 12th, 13th and 15th minor diagonals, while those from the 2nd to 11th contain only zero values, as do those from the 15th to 182th. Moreover, the matrix W is a block-tridiagonal matrix with 14 blocks of dimension 13×13 , with each block being tridiagonal itself. We next specify Q in (3) following the construction discussed in Leroux et al. [2000], that is, we set $Q(\tilde{\zeta}_t, W) = \tilde{\zeta}_t(\text{diag}(W\mathbf{1}) - W) + (1 - \tilde{\zeta}_t)\mathbb{I}_I$, where \mathbb{I}_I is the I -dimensional identity matrix and $\mathbf{1}$ is an I -dimensional vector of ones. Let d_i be the number of neighbors of site i . The matrix $(\text{diag}(W\mathbf{1}) - W)$ has elements equal to d_i if $i = j$, equal to -1 if i and j are neighbors ($i \sim j$), and equal to 0 otherwise. Here, parameter $\tilde{\zeta}_t$ controls the spatial autocorrelation structure: $\tilde{\zeta}_t = 1$ corresponds to the intrinsic CAR prior [Besag et al., 1991], where the conditional expectation is the mean of the random effects in geographically adjacent areal units. On the other hand, $\tilde{\zeta}_t = 0$ corresponds to independent random effects. The class of CAR models is large; see further detail in Besag [1974], Cressie [1993], Kaiser and Cressie [2000], Cressie and Wikle [2015] and references therein.

We introduce next the concept of *regime*. Given the nature of the data, we do not actually expect the parameters of the model to vary at each time t . Instead we expect to observe different states (called regimes), each with a specific set of parameters. The choice of the number of regimes is based on information about the evolving dynamics of the system. In our specific application, we assume the number of regimes to be based on the days of the

week (weekday/weekend), and on the period of the day (night/day). The regime indicators are denoted by $r_t \in \{1, \dots, n_R\}$, for $t = 1, \dots, T$, where n_R is the number of regimes allowed in the model. In light of the previous discussion, we assume some of the model parameters to be regime-specific, namely the harmonic regression coefficients: at each location i , we have $\beta_{i1}, \dots, \beta_{in_R}$. In addition, we consider n_R I -dimensional vectors of spatial random effects, $\mathbf{u}_1, \dots, \mathbf{u}_{n_R}$, as well as regime-specific scaling parameters $\tau_1^2, \dots, \tau_{n_R}^2$ and observation variances $\sigma_{\epsilon_1}^2, \dots, \sigma_{\epsilon_{n_R}}^2$. Finally, the parameters of the spatial precision matrix Q are also regarded as regime-specific, $\zeta_1, \dots, \zeta_{n_R}$. Using the correspondence between time point t and the regime present at that time r_t , we have that, at each t , $\tilde{\beta}_{it} = \beta_{ir_t}$, $\tilde{\mathbf{u}}_t = \mathbf{u}_{r_t}$ and $\tilde{\zeta}_t = \zeta_{r_t}$. This implies a substantial reduction in the number of model parameters.

Conditionally on regimes, we can rewrite the model as follows:

$$Y_{it} \mid \mathbf{x}_t, \beta_{ir_t}, u_{ir_t} = \mathbf{x}'_t \beta_{ir_t} + u_{ir_t} + \epsilon_{it}, \quad \epsilon_{it} \stackrel{\text{ind}}{\sim} \mathbf{N}(0, \sigma_{\epsilon_{r_t}}^2)$$

$$\mathbf{u}_{r_t} \mid \tau_{r_t}^2, Q(\zeta_{r_t}, W), \zeta_{r_t} \sim \mathbf{N}_I(\mathbf{0}, \tau_{r_t}^2 Q(\zeta_{r_t}, W)^{-1})$$

where each β_{ir_t} is K -dimensional, while \mathbf{u}_{r_t} is an I -dimensional parameter vector. The marginal priors for the parameters, as well as the whole model specification, are given in Section 3.3.

3.2 Areal Product Partition Model (aPPM)

We next discuss the time-varying spatial clustering structure component of the proposed model for the I time series of responses across regions. As commonly done in Bayesian nonparametrics, we define a clustering model by considering a prior distribution for the random partition parameter $\rho_r = \{C_1^r, C_2^r, \dots, C_{K_r}^r\}$ that denotes the partition of areas $\{1, 2, \dots, I\}$ in the sample at regime r . We define a prior distribution by building on product partition models [PPM, see, e.g., Quintana and Iglesias, 2003], and by modifying the spatially-oriented PPM proposed in Hegarty and Barry [2008]. To explain the proposal, we recall these models here. Under a PPM, the distribution on a partition ρ of a set of indices

$[I] = \{1, \dots, I\}$ is constructed in terms of a *cohesion* function for any subset $C \subset [I]$, which measures the strength of prior belief that the elements of C are to be grouped together. The PPM prior is thus expressed as

$$p(\rho = \{C_1, \dots, C_K\}) = \mathcal{K} \prod_{j=1}^K c(C_j), \quad \rho \in \mathcal{P}([I])$$

where $\mathcal{P}([I])$ denotes the set of all partitions of $[I]$ and \mathcal{K} is an appropriate normalizing constant depending on the cohesion function. A typical choice of cohesion function is $c(C_j) = \kappa \times \Gamma(n_j)$, with $n_j = |C_j|$, for $j = 1, \dots, K$ from which we recover the exchangeable partition probability function (EPPF) corresponding to the Dirichlet process (DP) with mass parameter $\kappa > 0$.

Recent developments in the study of PPMs have explored the possibility of adding additional prior information to the definition of c , such as covariates [Müller et al., 2011, Page and Quintana, 2016]. In our approach, we include the information about the areal structure of the data, and we do so by following the idea of Hegarty and Barry [2008], who introduce the notion of *boundary length* $\ell^j(i)$ of the i -th areal unit belonging to the cluster C_j as the number of neighbors of i that do not belong to C_j , for $j = 1, \dots, K$. The boundary length of a cluster C_j is computed as the sum of the boundary length of each areal unit in C_j . The model by Hegarty and Barry [2008] is thus given by

$$p(\rho = \{C_1, \dots, C_K\} \mid \xi) = \mathcal{K}(\xi, I) \prod_{j=1}^K e^{-\xi \sum_{i \in C_j} \ell^j(i)}, \quad (4)$$

where the normalizing constant $\mathcal{K}(\xi, I)$ is a function of I and of the positive hyperparameter ξ , so that

$$\frac{1}{\mathcal{K}(\xi, I)} = \sum_{\rho \in \mathcal{P}([I])} \prod_{j=1}^K e^{-\xi \sum_{i \in C_j} \ell^j(i)}.$$

Our proposed model combines the DP-based PPM and the spatial version of Hegarty and Barry [2008], with the difference that we consider as neighbors the eight areal units

surrounding $i \in [I]$, and not just the ones with a common side. Concretely, we consider

$$p(\rho = \{C_1, \dots, C_K\} \mid \kappa, \xi) = \mathcal{K}(\kappa, \xi, I) \kappa^K \prod_{j=1}^K \Gamma(n_j) e^{-\xi \sum_{i \in C_j} \ell^j(i)}, \quad (5)$$

where $\mathcal{K}(\kappa, \xi, I)$ is now a function of the positive hyperparameters κ , ξ and the number I of items to cluster. Compared to (4), prior (5) introduces an additional term, that coincides with that of the product form arising from the Dirichlet process prior when written in PPM form. In particular, following the notation in Hegarty and Barry [2008], the normalizing constant $\mathcal{K}(\kappa, \xi, I)$ is such that

$$\frac{1}{\mathcal{K}(\kappa, \xi, I)} = \sum_{\rho \in \mathcal{P}([I])} \prod_{j=1}^K \kappa \Gamma(n_j) e^{-\xi \sum_{i \in C_j} \ell^j(i)} \quad (6)$$

Thus, the number of clusters a priori grows with κ . On the other hand, ξ is related to spatial association by penalizing excessive spatial disconnectedness between subsets, in the sense that a larger ξ encourages smaller boundary lengths, and hence fewer clusters. The combination of both approaches strikes a balance between a “rich gets richer” DP-based clustering and a spatially-oriented setting proposed by Hegarty and Barry [2008]. As shown in Appendix B, we conduct simulation studies aimed at understanding the intertwining role of κ and ξ in controlling the prior partition structure.

To further understand the partition structure imposed by the proposed model (5), set $\eta = \exp(-\xi) \in (0, 1)$ and consider one, two or three areas. Table 1 shows the prior probability for different configurations given by the proposed prior distribution, up to a normalising constant. When $\eta = 1$ (equivalently, $\xi = 0$), the partition probabilities reduce to the DP prior case. This means that, a-priori, $\kappa > 1$ will assign more probability to partitions composed of singletons, while $0 < \kappa < 1$ to the partition with only one cluster. Considering a fixed value of $\kappa > 1$, similar considerations can be made for the value of η . Notice that the partition with one cluster is always favored when $\kappa \leq 1$ and that, in the case of three areas depicted in Table 1, two different areal configurations are allowed, yielding different a-priori probabilities. In particular, the partition with three clusters is penalized more when

Table 1: Prior probabilities (up to adequate normalising constants) for different configurations of one, two or three adjacent areal units. The probabilities are expressed as function of the mass parameter κ and the boundary length parameter $\eta = \exp(-\xi)$.

# areal units	Configuration	Partition	Prior probability \propto				
1	<table border="1" style="display: inline-table; vertical-align: middle;"><tr><td>1</td></tr></table>	1	{1}	1			
1							
2	<table border="1" style="display: inline-table; vertical-align: middle;"><tr><td>1</td><td>2</td></tr></table>	1	2	{1, 2} {1}, {2}	κ $\kappa^2\eta^2$		
1	2						
3	<table border="1" style="display: inline-table; vertical-align: middle;"><tr><td>1</td><td>2</td><td>3</td></tr></table>	1	2	3	{1, 2, 3}	2κ	
		1	2	3			
		{1}, {2, 3}	$\kappa^2\eta^2$				
		{1, 3}, {2}	$\kappa^2\eta^4$				
		{1, 2}, {3}	$\kappa^2\eta^2$				
	{1}, {2}, {3}	$\kappa^3\eta^4$					
	<table border="1" style="display: inline-table; vertical-align: middle;"><tr><td>2</td><td>3</td></tr><tr><td>1</td><td></td></tr></table>	2	3	1		{1, 2, 3}	2κ
		2	3				
		1					
		{1}, {2, 3}	$\kappa^2\eta^4$				
{1, 3}, {2}		$\kappa^2\eta^4$					
{1, 2}, {3}	$\kappa^2\eta^4$						
{1}, {2}, {3}	$\kappa^3\eta^6$						

the areal units are not aligned, since in our 8-neighbors setting all units are in contact with each other. Secondly, the partitions with two clusters in the second scenario have the same prior probabilities, while in the first scenario the prior probability depends on the specific partition. The partition in which areas 1 and 3 are clustered together is less probable than the one in which 1 and 2 or 2 and 3 are clustered together. Moreover, when κ is fixed and $\eta \rightarrow +\infty$, the probability of the partition with one cluster tends to one. This simple study shows the spatial “local” effect of the parameter η on the clustering.

When the number of areal units is larger than $I = 3$, it is difficult to see analytically what this implies. We propose in this section a simulated example aimed at understanding the

properties of the distribution of the partition a-priori. We show results applied to a rectangular grid of size 14x13, the same as the one used in the Telecom data application, yielding $I = 182$ areal units. The sensitivity analysis reported below presents the distribution of the number of clusters and the properties of the partition a-priori under the proposed model. For comparison, we also consider the Hegarty and Barry [2008] prior. MCMC samples from this model follow easily from the Gibbs sampler algorithm in Appendix A by suitably dropping the likelihood and DP parts. For the proposed model, we fix κ to 1 so that the expected number of clusters under the regular DP prior is $\mathbb{E}(K_n) = \sum_{j=1}^I \kappa / (\kappa + j - 1) \approx 5.78$. We also select a grid of values for ξ for comparison; see Figures 3 and 4.

In Hegarty and Barry [2008], the authors report that their prior distribution induces partitions with fewer large clusters for large values of ξ and vice-versa, small values of ξ induce partitions with many clusters of reduced sizes. In particular, Figure 3 shows the prior distribution of the number of clusters for a grid of ξ values for the Hegarty and Barry [2008] prior setting. As we can observe, the distribution of the number of clusters is concentrated on lower values as the value of ξ increases.

The behavior of our partition prior is summarized in Figure 4 by reporting the prior distribution of the number of clusters. We can observe how the effect of ξ , as in the previous simulation, is to produce coarser partitions. However, this effect is incremented by the presence of the DP part in our prior specification, evident by comparing these results with Figure 3, where the prior number of clusters is, given the same value of ξ , much higher.

3.3 Regime- switching aPPM - Time varying spatial clustering

As mentioned in Section 1, we are interested in detecting which areal units share similar temporal patterns. For this reason, the strategy we develop below builds the clustering structure on the array of coefficients $\beta = [\beta_{ir_t}]$, for $i \in [I]$, $t \in [T]$, and associated regime $r_t \in [n_R]$, in the spirit of Bayesian nonparametric priors of discrete nature. Thanks to the introduction of the concept of model regimes, the clustering induced on the observations via β is able to

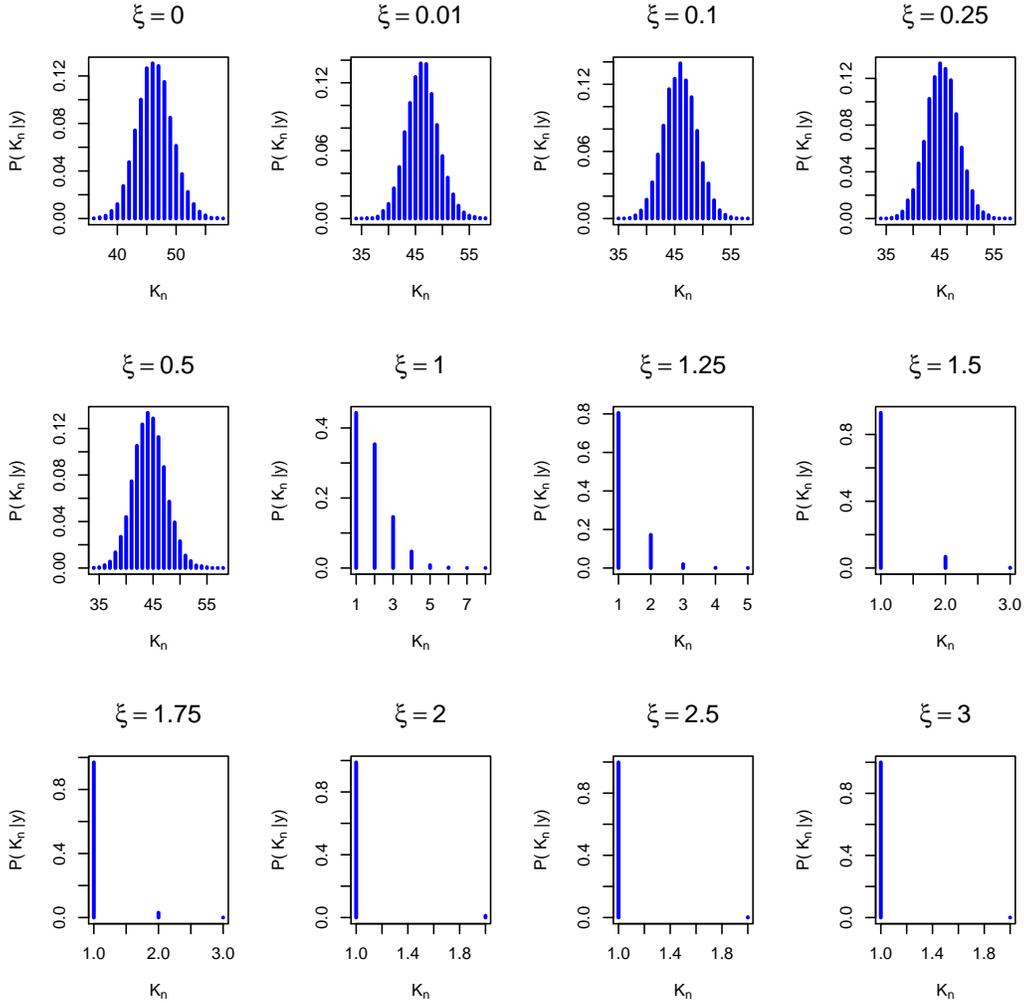


Figure 3: Distribution of the number of clusters K_n under the prior for ρ as in **Hegarty and Barry (2008)**, for different values of ξ .

reflect changes appearing through time, allowing for a regime-specific prior distribution for the partition of areas.

Firstly, we elaborate on the concept of regime and its relationship with the clustering of observations. A regime r_t at time $t \in [T]$ is associated to a partition of the areas indexed in $[I]$ indicated as $\rho_{r_t} = \{C_1^{r_t}, \dots, C_{K_{r_t}}^{r_t}\}$. The number of clusters for each regime-specific partition is denoted by K_{r_t} . Because we allow for the same regime to exist at multiple

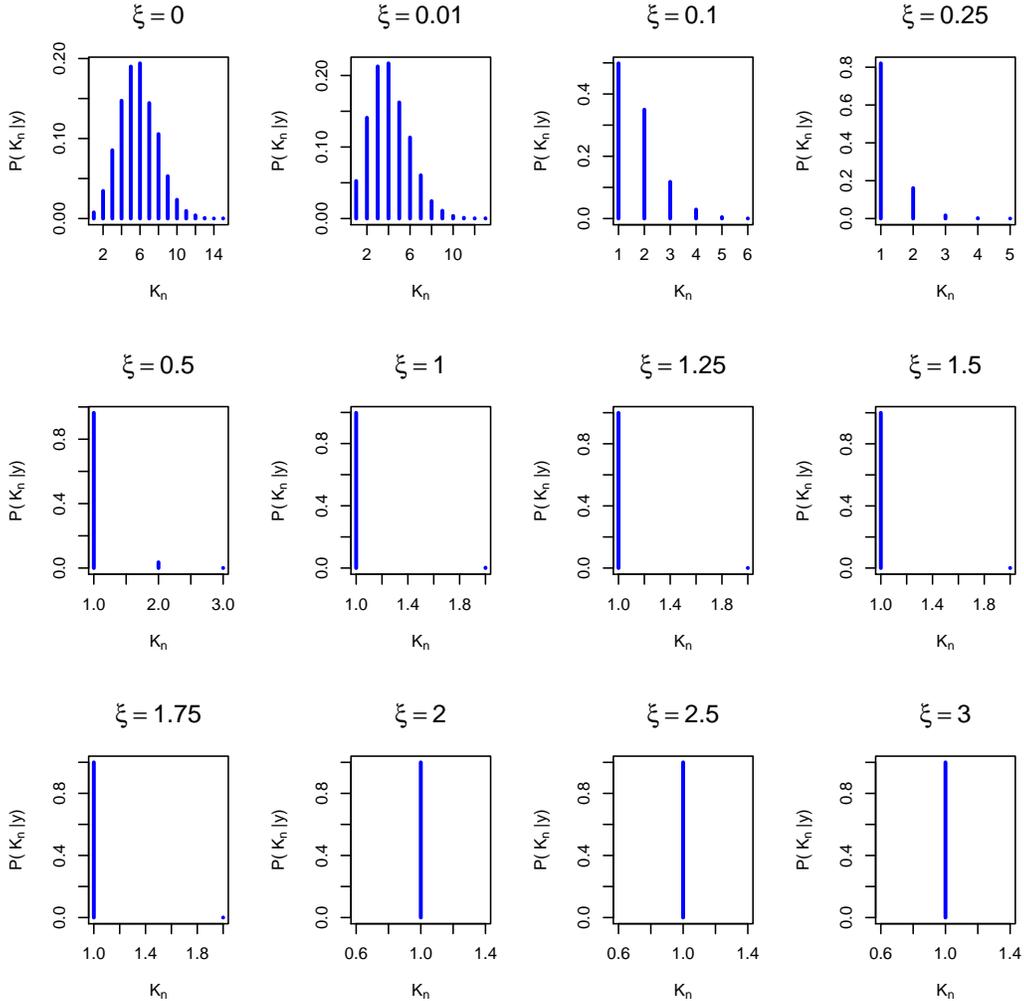


Figure 4: Distribution of the number of clusters K_n under the our prior for ρ (see (5)), which includes a DP term, for different values of ξ . The mass parameter κ is fixed to 1.

time points over the time period under study, we must permit the same partition ρ_{r_t} to exist at these time points, effectively exploiting the division of the set $[T]$ of time points into $M \geq n_R$ non-overlapping sets. For instance, in our application, we distinguish between night and day regimes, as well as weekday/weekend, therefore considering $n_R = 4$ distinct regimes. However, we consider $M = 15$ non-overlapping intervals, since we have two weeks of observations, and there are two changes within each day to separate day by night

(see Figure 5). Of course, this choice is suggested by the specific application considered here, but either simpler or more general choices could be considered. Changes in the regime status are identified by the time points $\bar{t}_0, \dots, \bar{t}_M$, dividing the time set into non-overlapping intervals, such that:

$$[T] = \{\bar{t}_0, 2, \dots, \bar{t}_1\} \cup \{\bar{t}_1 + 1, \dots, \bar{t}_2\} \cup \dots \cup \{\bar{t}_{M-1} + 1, \dots, \bar{t}_M\}, \quad (7)$$

where $\bar{t}_0 = 1, \bar{t}_M = T$ and $\bar{t}_1 < \bar{t}_2 < \dots < \bar{t}_{M-1} < \bar{t}_M$. Depending on the application under study, one might possess prior information on when regimes change. However, in many situations such as the one presented here, the time points $\bar{t}_1, \dots, \bar{t}_{M-1}$ are not deterministically known. Hence, we impose a prior distribution over a range of possible time points around 7am and 7pm within each day of the week. Recalling that $\bar{t}_0 = 1$ and $\bar{t}_M = T$, the center of the change-point intervals are denoted by λ_m , for $m = 1, \dots, M - 1$. Specifically, we assume a discrete uniform prior distribution over the $2n_\lambda + 1$ discrete time points centred over $\lambda_m \in \{7\text{am}, 7\text{pm}\}$, for $m = 1, \dots, M - 1$, allowing to reasonably span those hours in the day when a regime shift might be observed, due for example to commuting work/home hours and school or offices opening times. For example we could set $n_\lambda = 4$ and assume \bar{t}_1 , the first regime change-point, to be uniformly distributed over the time points corresponding to 6am, 6:15am, 6:30am, 6:45am, 7am, 7:15am, 7:30am, 7:45am, and 8am, representing the prior belief of the city awakening period. Of course, we always assume (7) to be a partition of $[T]$. This is imposed by selecting an integer n_λ such that the support of each variable \bar{t}_m is $\{\lambda_m - n_\lambda, \dots, \lambda_m + n_\lambda\}$. Notice that, given the values \bar{t}_m , for $m = 0, \dots, M$, the regime status r_t at each time point is known deterministically.

Finally, we assume that, conditionally on all the change-points $\bar{\mathbf{t}} = (\bar{t}_0, \dots, \bar{t}_M)$, the n_R regime-specific partitions $\rho_1, \dots, \rho_{n_R}$ are independent, each distributed according to (5). Each regime-specific partition $\rho_r = \{C_1^r, \dots, C_{K_r}^r\}$, for $r \in [n_R]$ can be equivalently represented through the introduction of a regime-specific vector of allocation variables $\mathbf{s}^r = (s_1^r, \dots, s_I^r)$. Furthermore, a vector of unique values $\boldsymbol{\beta}_r^* = (\beta_{1r}^*, \dots, \beta_{K_r r}^*)$ for each regime can be linked to $\tilde{\boldsymbol{\beta}}$, and in such a way to the observations, so that $s_i^r = j \iff$

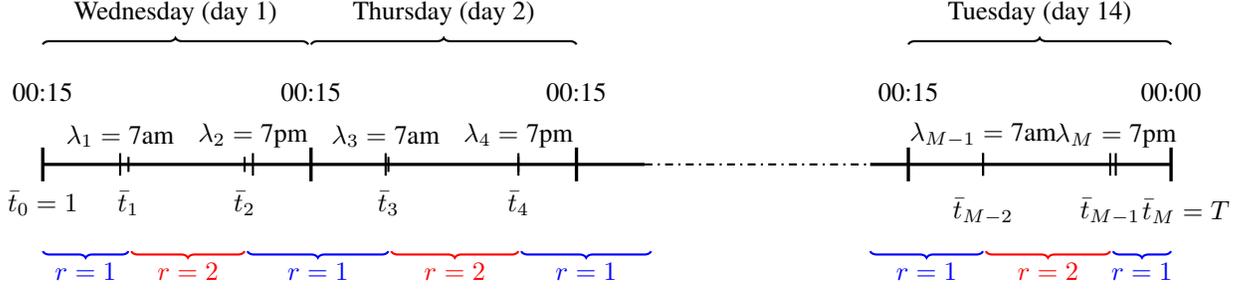


Figure 5: Illustration of the regime scheme in the case under study. Throughout the time interval, the regimes are depicted in different colors, here indicating night/day separation. Notice how the regime interval is spanned by the change-points \bar{t}_r , which are not necessarily coinciding with the central time points λ_r . The total number of regimes is 4. The two regimes in the weekend are not explicitly visible in the above plot because of the space limit of the figure.

$$\tilde{\beta}_{it} = \beta_{jr}^* \iff i \in C_j^r \text{ and } r = r_t.$$

After we have introduced the allocation vector $\mathbf{s}^r = (s_1^r, \dots, s_J^r)$, and the set of unique parameter values β_r^* , we can describe the predictive distribution of \mathbf{s}^r . For notational convenience, we temporarily omit the index r indicating the regime. Consider the partition $\rho^i = \{C_1^i, \dots, C_{K^i}^i\}$ obtained by clustering the first i elements into K^i clusters. The predictive law of a new element $i+1$ can be computed as follows:

$$P(s_{i+1} = j \mid s_1, \dots, s_i) = \begin{cases} \frac{p(\rho^{i+1} = \{C_1^i, \dots, C_j^i \cup \{i+1\}, \dots, C_{K^i}^i\} \mid \kappa, \xi)}{p(\rho^i = \{C_1^i, \dots, C_{K^i}^i\} \mid \kappa, \xi)} \propto n_j^i e^{-\xi \ell^j(\{i+1\})}, & j = 1, \dots, K^i \\ \frac{p(\rho^{i+1} = \{C_1^i, \dots, C_{K^i}^i, \{i+1\}\} \mid \kappa, \xi)}{p(\rho^i = \{C_1^i, \dots, C_{K^i}^i\} \mid \kappa, \xi)} \propto \kappa e^{-\xi \ell^j(\{i+1\})}, & j = K^i + 1, \end{cases} \quad (8)$$

where $n_j^i = |C_j^i|$ is the j -th cluster size before we assign the $(i+1)$ -th observation, and K^i is the number of clusters identified by (s_1, \dots, s_i) so that $K^i + 1$ identifies the new cluster label. To recover the first line of formula (8) above, note that the ratio there is equal to

$$\frac{\mathcal{K}^r(\kappa, \xi, i+1) \Gamma(n_j^i + 1) e^{-\xi \sum_{m \in C_j^r \cup \{i+1\}} \ell^j(m)}}{\mathcal{K}^r(\kappa, \xi, i) \Gamma(n_j^i) e^{-\xi \sum_{m \in C_j^r} \ell^j(m)}} = \frac{\mathcal{K}^r(\kappa, \xi, i+1)}{\mathcal{K}^r(\kappa, \xi, i)} n_j^i \frac{e^{-\xi \sum_{m \in C_j^r} \ell^j(m) - \xi \ell^j(\{i+1\})}}{e^{-\xi \sum_{m \in C_j^r} \ell^j(m)}},$$

so that the ratio $\mathcal{K}^r(\kappa, \xi, i+1)/\mathcal{K}^r(\kappa, \xi, i)$ does not depend on j . Similar calculations hold

for the second line in (8).

Finally, we impose the following prior distribution for the vector of unique values β_r^* :

$$\beta_{1r}^*, \dots, \beta_{K_r r}^* \mid \rho_r, \boldsymbol{\mu}_{\beta_r}, \boldsymbol{\Sigma}_{\beta_r} \stackrel{\text{iid}}{\sim} \mathbf{N}_K(\boldsymbol{\mu}_{\beta_r}, \boldsymbol{\Sigma}_{\beta_r}), \quad r = 1, \dots, n_R,$$

$$\boldsymbol{\mu}_{\beta_r}, \boldsymbol{\Sigma}_{\beta_r} \sim \mathbf{N}_K(\boldsymbol{\mu}_{\beta_r} \mid \mathbf{m}_{\beta_r}, \boldsymbol{\Sigma}_{\beta_r}) \prod_{j=1}^K \text{inv-Gamma}(\sigma_{\beta_r j}^2 \mid a_{\boldsymbol{\Sigma}_{\beta_r}}, b_{\boldsymbol{\Sigma}_{\beta_r}}), \quad r = 1, \dots, n_R,$$

where $\boldsymbol{\Sigma}_{\beta_r} = \text{diag}(\sigma_{\beta_r 1}^2, \dots, \sigma_{\beta_r K}^2)$, $r = 1, \dots, n_R$. Here $\text{inv-Gamma}(\cdot \mid a, b)$ denotes the inverse gamma density with mean $b/(a-1)$. We note that the unique values of the array β_r^* , associated with the r -th regime, are shared by all those coefficients $\tilde{\beta}_{it}$ for which regime r is active, hence for all $t \in \{\bar{t}_m + 1, \dots, \bar{t}_m\}$. We also assume independence among the β^* 's parameters across different regimes r .

The final model, which we refer to as regime-switching areal PPM (RS-aPPM), can be described as follows:

$$Y_{1t}, \dots, Y_{It} \mid \mathbf{x}_t, \beta_{1r}^*, \dots, \beta_{K_r r}^*, \rho_r = \{C_1^r, \dots, C_{K_r}^r\}, \mathbf{s}^r, \mathbf{u}_r, \sigma_{\epsilon_r}^2, r = r_t$$

$$\stackrel{\text{ind}}{\sim} \prod_{j=1}^{K_r} \prod_{i \in C_j^r} \mathbf{N}(y_{it} \mid \mathbf{x}'_t \beta_{s_i^r}^* + u_{ir}, \sigma_{\epsilon_r}^2), \quad \text{for all } t : r_t = r, \quad (9)$$

$$\mathbf{u}_r \mid \tau_r^2, Q(\zeta_r, W) \sim \mathbf{N}_I(\mathbf{u}_r \mid \mathbf{0}, \tau_r^2 Q(\zeta_r, W)^{-1}), \quad r = 1, \dots, n_R, \quad (10)$$

$$\beta_{1r}^*, \dots, \beta_{K_r r}^* \mid \rho_r, \boldsymbol{\mu}_{\beta_r}, \boldsymbol{\Sigma}_{\beta_r} \stackrel{\text{iid}}{\sim} \mathbf{N}_K(\boldsymbol{\mu}_{\beta_r}, \boldsymbol{\Sigma}_{\beta_r}), \quad r = 1, \dots, n_R \quad (11)$$

$$\boldsymbol{\mu}_{\beta_r}, \boldsymbol{\Sigma}_{\beta_r} \sim \mathbf{N}_K(\boldsymbol{\mu}_{\beta_r} \mid \mathbf{m}_{\beta_r}, \boldsymbol{\Sigma}_{\beta_r}) \prod_{j=1}^K \text{inv-Gamma}(\sigma_{\beta_r j}^2 \mid a_{\boldsymbol{\Sigma}_{\beta_r}}, b_{\boldsymbol{\Sigma}_{\beta_r}}), \quad r = 1, \dots, n_R \quad (12)$$

$$\text{with } \boldsymbol{\Sigma}_{\beta_r} = \text{diag}(\sigma_{\beta_r 1}^2, \dots, \sigma_{\beta_r K}^2), \quad r = 1, \dots, n_R \quad (13)$$

$$\rho_1, \dots, \rho_{n_R} \stackrel{\text{iid}}{\sim} p(\rho_r \mid \kappa, \xi, \bar{\mathbf{t}}) = \mathcal{K}^r(\kappa, \xi, \mathbf{n}^r) \kappa^{K_r} \prod_{j=1}^{K_r} \Gamma(n_j^r) e^{-\xi \ell(C_j^r)} \quad (14)$$

$$\bar{t}_m \stackrel{\text{iid}}{\sim} \text{Unif}\{\lambda_m - n_\lambda, \dots, \lambda_m + n_\lambda\}, \quad m = 1, \dots, M-1 \quad (15)$$

$$\text{with } \{1, \dots, T\} = \{\bar{t}_0, 2, \dots, \bar{t}_1\} \cup \{\bar{t}_1 + 1, \dots, \bar{t}_2\} \cup \dots \cup \{\bar{t}_{M-1} + 1, \dots, \bar{t}_M\}$$

We complete the prior specification with

$$\tau_r^2 \stackrel{\text{iid}}{\sim} \text{inv-Gamma}(a_{\tau_r^2}, b_{\tau_r^2}), \quad r = 1, \dots, n_R, \quad (16)$$

$$\sigma_{\epsilon_r}^2 \stackrel{\text{iid}}{\sim} \text{inv-Gamma}(a_{\sigma_{\epsilon_r}^2}, b_{\sigma_{\epsilon_r}^2}), \quad r = 1, \dots, n_R. \quad (17)$$

Furthermore, prior independence is assumed among the parameters in the different equations above. Recall also that $Q(\zeta_r, W) = \zeta_r(\text{diag}(W\mathbf{1}) - W) + (1 - \zeta_r)\mathbb{I}_I$, where W is the proximity matrix, as previously introduced in Section 3.1. We could assume ζ_r 's random, e.g., beta-distributed. However, it is well-known (see, for instance, Banerjee et al. [2014], Section 6.4.3.3, or Goicoa et al. [2018]) that this leads to non-identifiability issues. For this reason, in the data application we have fixed $\zeta_r = 0.95$ for each regime r , encouraging spatial association, and have assumed informative marginal priors for τ_r^2 and $\sigma_{\epsilon_r}^2$. See Section 4 for the specific choice.

Let us denote by ϕ the vector containing all the model parameters, that is $\phi = (\mathbf{y}^{mis}, \beta, \boldsymbol{\rho}, \mathbf{s}, \bar{t}, \mathbf{u}, (\tau_1^2, \dots, \tau_{n_R}^2), (\sigma_{\epsilon_1}^2, \dots, \sigma_{\epsilon_{n_R}}^2), \boldsymbol{\mu}_\beta, \boldsymbol{\Sigma}_\beta)$, where $\boldsymbol{\rho} = (\rho_1, \dots, \rho_{n_R})$, $\mathbf{s} = (\mathbf{s}^1, \dots, \mathbf{s}^{n_R})$ and $\bar{t} = (\bar{t}_0, \dots, \bar{t}_M)$. To obtain posterior samples from the full joint posterior distribution $\pi(\phi | \mathbf{y}^{obs})$, we implement a sequence of Metropolis-within-Gibbs steps. See Appendix A for its full description. Note that since there are missing values in the log-Erlang numbers, denoted by \mathbf{y}^{mis} , we incorporate them in the parameters to be simulated from the full conditionals, i.e. ϕ contains \mathbf{y}^{mis} . See step 1. in the MCMC algorithm in Appendix A.

3.4 Summary of the simulation study

We perform extensive simulation studies investigating the effect of prior elicitation on the clustering estimation and posterior distributions of the parameters of interest. We provide in this section a summary of these simulations, while more details are reported in Appendix B.

We simulate data from (9)-(10), varying the values of the parameters in three different scenarios. The aim of this simulation study is to show how the areal information included in the cohesion function (5) can help recover the clustering structure.

In the first and second examples, only one regime is considered in the simulations process ($n_R = 1$). The first setting has no missing data, while the second presents missing data. In both cases, two underlying clusters are considered that are being *contaminated*, that is one areal unit associated to a cluster is totally surrounded by areal units associated to the other cluster (see Figure 11). In the third simulation setting, data are simulated from the same likelihood as before but from a multi-regime setting. In particular, the underlying number of regimes is $n_R = 2$, and the regime-specific clustering structure is as shown in Figure 20.

We fit model (9)-(17), though we also assume the variables ζ_r in the definition of $Q(\tilde{\zeta}_r, W)$ in (10) as random, with independent beta distributions, for $r = 1, \dots, n_R$. In the third simulation example, we assume the marginal prior (15) and show the posterior distribution of the change points \bar{t}_m (see Figure 26). By varying the hyperparameter values, we find the posterior inference around these parameters to be quite robust.

Our model is able to recover the areal clustering in all three simulation scenarios. However, we are not always able to identify separately $\tau^2, \sigma_\epsilon^2, \zeta$, due to non-identifiability issues (see, for instance, Banerjee et al. [2014], Section 6.4.3.3, or Goicoa et al. [2018]). In particular, this leads to Markov chains that are highly correlated and multimodal, with the marginal posterior possibly concentrated on values different from the truth. In the presence of missing data, cluster estimates recover the truth when the data are missing at multiple time points. On the other hand, if a whole trajectory of log-Erlang data is missing in some areal units, despite the spatial prior, the missing trajectories are not clustered correctly. See Appendix B. In the multi-regime example, the change-points (see Figure 26) are recovered satisfactorily, with the posterior mode of the distribution corresponding to the values used in the data simulation.

Despite the very good simulation behavior just commented, estimation of change-points for the actual data produced counter-intuitive results, with posterior distributions tending to concentrate on the edges of their corresponding support ranges; we report such inference in Figure 29. This behaviour could be caused by the model attempting to accommodate changepoints that are common across areal units, disregarding a possible area-specific effect

which might be present in the data at hand. As shown in previous spatio-temporal analysis [Rajala et al., 2023], the inclusion of areal-specific information in the model is able to improve changepoint detection. However, due to the already large number of parameters involved in the proposed model, we deem this to be unfeasible for the current framework. Nevertheless, this approach represents an interesting avenue for future research. Therefore, for the application discussed in the next section, we have opted for fixing the change-points at the corresponding prior centres λ_m , for $m = 1, \dots, M - 1$.

4 Application to Telecom data

In this section we fit our model to the Telecom data described in Section 2. Recall the log-Erlang values were previously standardized. We assume (9)-(10) with \mathbf{x}_t given in (2) and we fix $n_R = 4$ regimes. The prior is as defined in (11) – (14) and (16) – (17) but fixing the change-points at the corresponding prior centres λ_m , for $m = 1, \dots, M - 1$, as explained earlier. The diagonal elements of Σ_{β_r} are a-priori inverse Gamma distributed with mean and variance equal to 1 and 0.01, respectively. The hyperparameters $a_{\tau_r^2}$, $b_{\tau_r^2}$, $a_{\sigma_{\epsilon_r}^2}$, $b_{\sigma_{\epsilon_r}^2}$ in (16) and (17) are fixed in order to get informative priors with means and variances equal to 1 and 0.1, respectively. The hyperparameters in the marginal prior for ρ_r in (14) are ξ and κ . From the analytic expression of this prior, and the prior simulation study, we know that the number of clusters increases with κ , while it decreases with ξ . Given the amount of data allocated to each regime, we found that the corresponding likelihood terms have predominant weight in the marginal posterior distributions of ρ_r . Therefore, in an attempt to induce some parsimony in the resulting clustering, we conducted the analysis fixing $\xi = 2$ and $\kappa = 1$, reflecting a very informative prior on K_I as seen in Figure 4.

We run the MCMC for model (9)-(17) with fixed change-points for a total of 50,000 iterations, after a burn-in of 5,000 and thinning by 2. For each regime, we report a point estimate of the random partition for areal units, minimizing the posterior expectation of the variation of information (VI) loss function with equal missclassification cost parameters. Since the

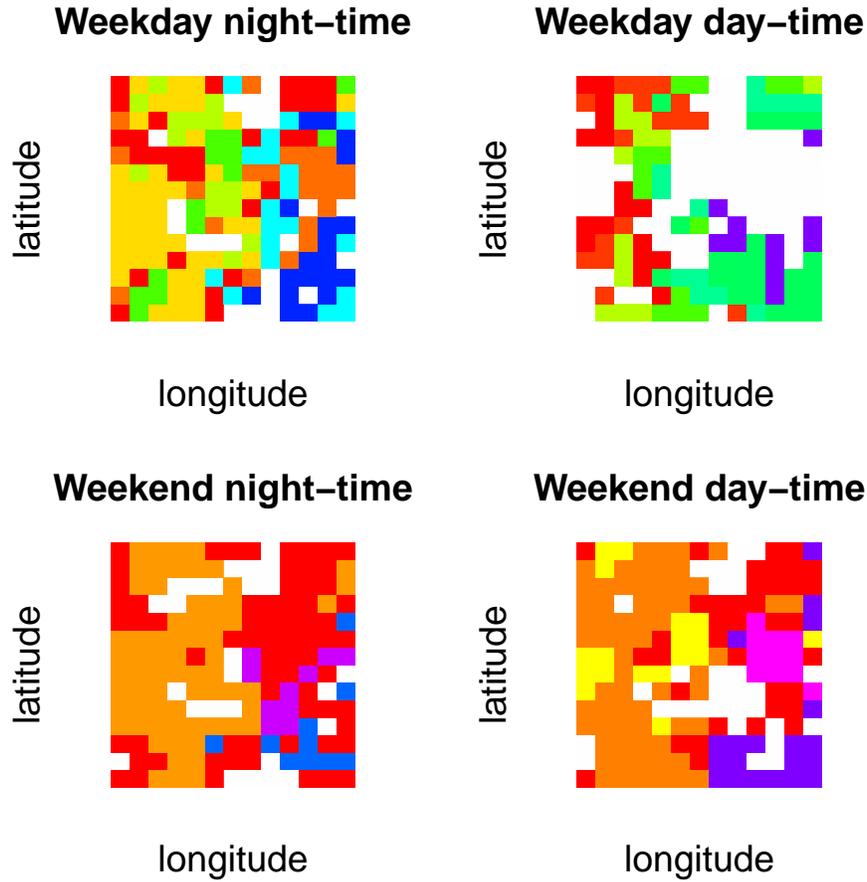


Figure 6: Telecom data. Posterior estimate of the random partition ρ_r , for $r = 1, \dots, n_R = 4$, given by minimizing the VI loss function; hyperparameters in the random partitions prior are such as $\xi = 2$, $\kappa = 1$. Areal units in clusters of size smaller than ten are left uncolored. Each color corresponds to a cluster, with the color scale not reflecting the intensity of a parameter.

cardinality of the visited partitions is quite large, as suggested by Wade and Ghahramani [2018], from the MCMC estimate of the posterior co-clustering matrix, we consider all the partitions designed by a hierarchical clustering algorithm with a distance equal to 1- the posterior probability of co-clustering and average linkage. Calculations were done via the R package `salso` [Dahl et al., 2022]; see also <https://CRAN.R-project.org/package=salso>.

In Figure 6, each cluster is identified by a different color. For visualization purposes, areal

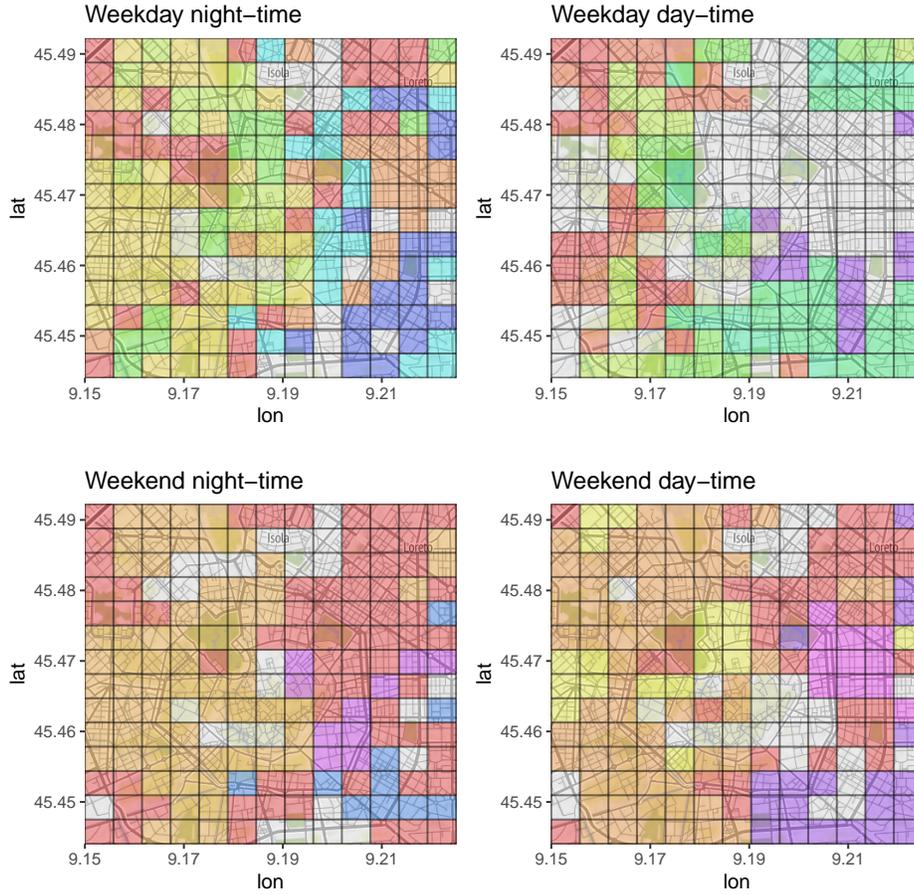


Figure 7: Telecom data. Posterior estimate of the random partition ρ_r , for $r = 1, \dots, n_R = 4$, given by minimizing the VI’s loss function. Areal units in clusters of size smaller than ten are left uncolored. Each color corresponds to a cluster, with the color scale not reflecting the intensity of a parameter. A map of the total area is superimposed.

units in clusters of size smaller than ten are left uncolored. We can observe how clusters of large sizes identify regions of the metropolitan area of Milan corresponding to the centre, external rings, and specific hotspots in the map. The grouping of the areal unit changes between regimes, reflecting the different types of trajectories observed. Figure 7 displays the same plot as in Figure 6, where the cluster estimates are superimposed over the map of the whole area. The estimated clustering of trajectories is also reported in Figure 8, where the

trajectories are colored according to the VI loss partition at each regime.

Figures 6 and 7 show some interesting characteristics. In the regime corresponding to weekend day-time, the Duomo area, the highly commercial street of Corso Vittorio Emanuele and nearby areal units are blank, i.e., they do not form a large cluster. Instead big clusters are made by contiguous areal units overlapping the more external rings. For instance, we see a (blue) cluster at the bottom right corner, around Porta Romana and Piazzale Lodi. There is a large cluster around the area of Porta Venezia (violet), and then another large (red) cluster at the top right corner, including Piazzale Loreto. The west part of the city is split into two clusters, the largest of them overlapping the more external rings. For weekend night-time, the city seems to be cut in half by a vertical line separating the two larger clusters (the orange and the red clusters). During the weekday day-time, it is clear that there is a large part of the city that is split into small cluster (the grey area in the northern and eastern part), but there are clusters that split the external rings (two green clusters, the red cluster, the lemon yellow cluster). Finally, in Figure 7 at weekday night-time, we estimate the largest number of clusters in total for the four regimes and the cluster estimate we get is less homogeneous. For instance, there is a blue cluster at the bottom right corner, overlapping the external ring (viale Isonzo, piazzale Lodi, viale Umbria), a red cluster at the top right including piazzale Loreto, and a very large orange cluster in the western part. Note, however, that the total number of estimated clusters is 13 for weekday day-time, 15 for weekday night-time and weekend day-time, 30 for weekday day-time. For this last regime, comparison to Figure 6 shows that there are many clusters of size smaller than ten (left uncolored).

In order to understand the differences between the random partitions in the regimes, Figure 9 reports the posterior distribution of the Rand Index between ρ_i and ρ_j , $i \neq j$, a similarity measure for partitions, where values closer to 1 indicate partitions that are more similar. It is clear from the figure that all the cluster estimates show a high level of similarity, though weekend night-time seems the one less similar to all the others.

We include here the plots of the function of the posterior mean of $\mathbf{x}'_t \boldsymbol{\beta}_{ir_t}$, as a function of

t , for three different areas i 's, corresponding to Stazione Centrale (Central Station), Piazza Duomo and Piazzale Piola. See the corresponding plots in Figure 10, where the locations are shown in Figure 1. The plots suggest that each of these locations exhibit high or low activity, depending on specific periods. Duomo is very active on weekdays but less so during weekends, while Piola oscillates between high activity on weekends or low activity late at night.

We have underlined that, a priori, parameter ξ controls the number of clusters. We show that a posteriori the effect is not so strong. In particular, in Appendix B, Figures 27 and 28 show the point estimate of the clustering obtained under $\kappa = 1$ and $\xi = 1$. Table 2 shows a comparison between the partitions estimated by minimizing the VI loss functions, for each regime, when $\xi = 2$ and $\xi = 1$, keeping $\kappa = 1$. The partitions are compared in terms of estimated number of clusters K_I and similarity between partitions as measured by the Rand Index [RI, Rand, 1971]. A Rand Index close to 1 indicates a high similarity between the partitions. In our case, the lowest Rand Index is obtained in the Weekend night-time regime, with the value of 0.81, and reaches 0.94 in the weekend night-time. The number of clusters is similar between the two partitions at each regime, being the highest during the weekend day-time; however, of these 30 estimated clusters, only 5 have sizes larger than ten.

r	K_I		similarity
	$\xi = 2$	$\xi = 1$	RI
Weekday night-time	15	14	0.92
Weekday day-time	30	28	0.95
Weekend night-time	13	10	0.81
Weekend day-time	15	12	0.92

Table 2: Comparison between partitions estimated by minimising the VI loss function, for each regime, when $\xi = 2$ and $\xi = 1$. The Table shows the estimated number of clusters K_I (first two columns) and the similarity between partitions, quantified by the Rand Index (RI).

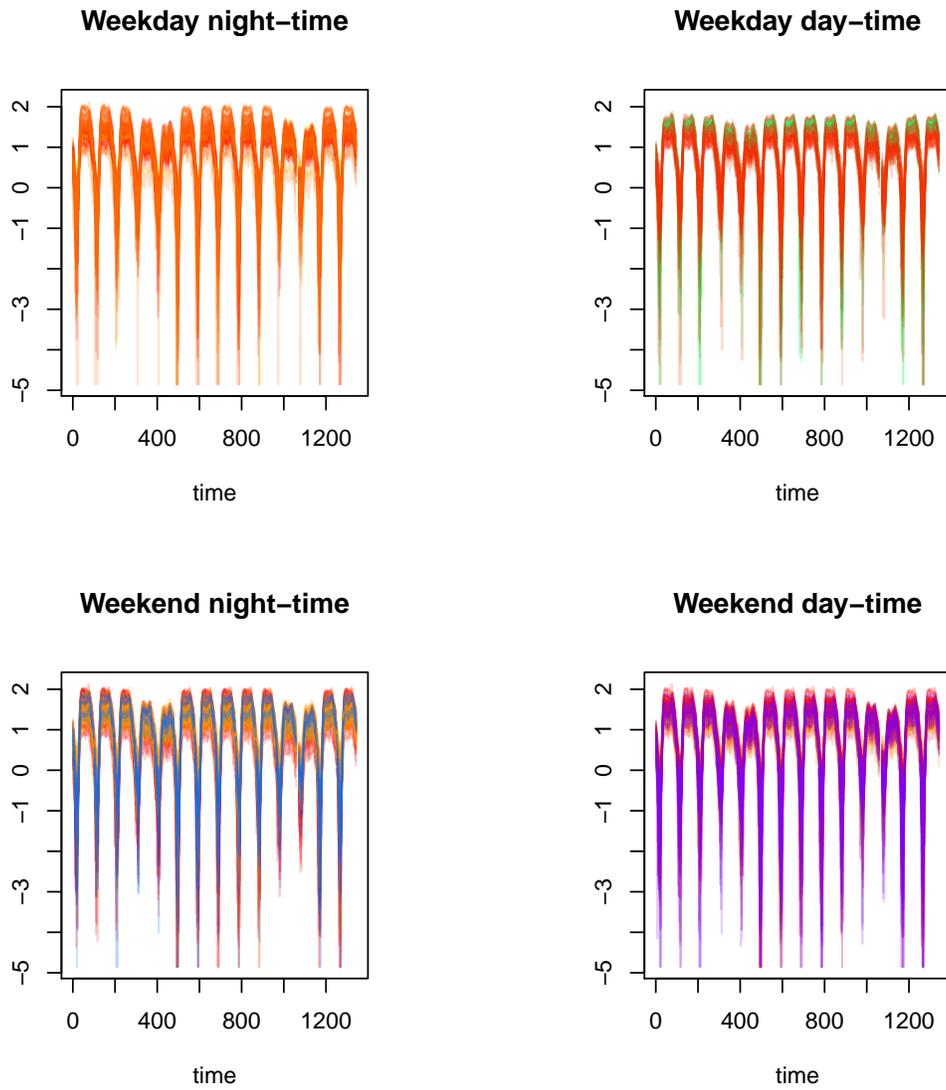
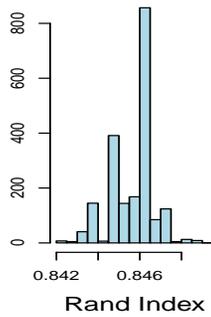
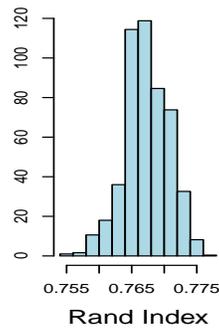


Figure 8: Telecom data. Observed trajectories colored according to the estimated VI partition.

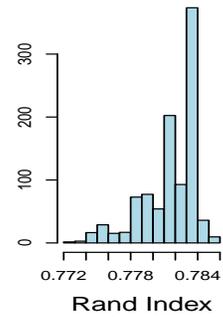
Regimes 1 VS 2



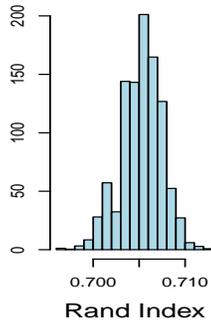
Regimes 1 VS 3



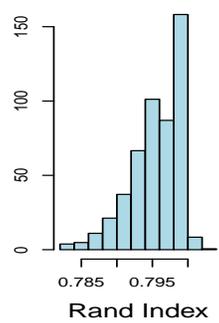
Regimes 1 VS 4



Regimes 2 VS 3



Regimes 2 VS 4



Regimes 3 VS 4

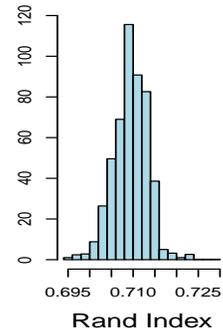


Figure 9: Telecom data. Posterior distribution of the Rand Index between ρ_i and ρ_j , $i \neq j$. Here $i = 1$ is weekday night-time, $i = 2$ weekday day-time, $i = 3$ weekend night-time and $i = 4$ weekend day-time.

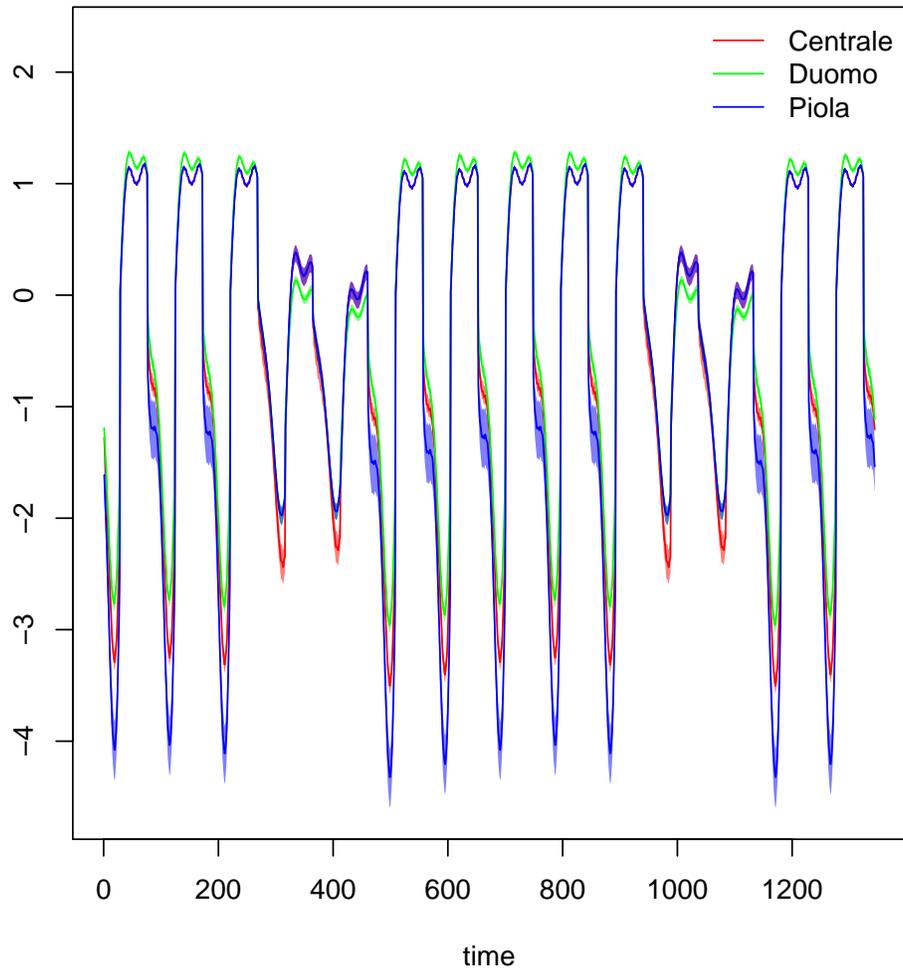


Figure 10: Telecom data. Posterior mean and 95% credible interval for $\mathbf{x}'_t \boldsymbol{\beta}_{ir_t}$, as a function of t , when i denotes the areal unit including Stazione Centrale, Piazza Duomo and Piazzale Piola.

5 Summary and Conclusions

Motivated by the analysis of mobile phone usage in part of the city of Milan, Italy, we propose a semi-parametric random partition model for the analysis of large spatio-temporal data. The model features a random partition prior distribution that combines the well-known DP with the HB specifications, providing a balance among spatially cohesive areal grouping and number and sizes of clusters. Due to the nature of the data, consisting of series of measurements every 15 minutes over the entire span of two weeks, the model also incorporates the notion of switching regimes, to reflect differences over weekday/night and weekend patterns of mobile phone usage.

Through extensive simulation studies we find that the model fares well when compared to other alternatives, including the random partition models corresponding to either the DP or the HB priors (i.e., not combined) and the models included in `CARBayesST` package available in R. These comparisons are included in Appendix B.

We would like to point out that an alternative to doing inference based on MCMC simulation is to use a Integrated Nested Laplace Approximations (INLA, Rue et al. [2009]). INLA has become increasingly popular in the analysis of spatio-temporal data, also thanks to the R-INLA package. However, while R-INLA can fit many different spatio-temporal models, it does not provide a way to implement a model equipped with a random partition.

A limitation of our model, in fact shared with many related random partition models is the computational burden required to implement posterior simulation via MCMC. A possible topic for future research is the adoption of divide and conquer techniques that split the data in smaller segments that can be dealt with in parallel, to be later suitably combined to produce a reasonable approximation to the actual posterior distribution.

Acknowledgments

Fernando Quintana was partially supported by grant FONDECYT 1220017. Alessandra Guglielmi has been partially supported by MUR, PRIN project 2022CLTYP4. She also acknowledges the support by MUR, Grant Dipartimento di Eccellenza 2023–2027.

References

- Craig Anderson, Duncan Lee, and Nema Dean. Identifying clusters in bayesian disease mapping. *Biostatistics*, 15(3):457–469, 2014.
- Cecilia Balocchi, Edward I George, and Shane T Jensen. Clustering areal units at multiple levels of resolution to model crime incidence in philadelphia. *arXiv preprint arXiv:2112.02059*, 2021.
- S. Banerjee, B. P. Carlin, and A. E. Gelfand. *Hierarchical modeling and analysis for spatial data*. Chapman and Hall/CRC, 2014.
- Julian Besag. Spatial interaction and the statistical analysis of lattice systems. *Journal of the Royal Statistical Society. Series B (Methodological)*, pages 192–236, 1974.
- Julian Besag. Statistical analysis of non-lattice data. *Journal of the Royal Statistical Society. Series D (The Statistician)*, 24(3):pp. 179–195, 1975. ISSN 00390526. URL <http://www.jstor.org/stable/2987782>.
- Julian Besag, Jeremy York, and Annie Mollié. Bayesian image restoration, with two applications in spatial statistics. *Annals of the Institute of Statistical Mathematics*, 43(1):1–20, Mar 1991. ISSN 1572-9052. doi: 10.1007/BF00116466. URL <https://doi.org/10.1007/BF00116466>.
- Annalisa Cadonna, Andrea Cremaschi, Alessandra Guglielmi, et al. Bayesian modeling for

- large spatio-temporal data: an application to mobile networks. In *SIS 2019-Smart Statistics for Smart Applications*, pages 691–696. Pearson, 2019.
- N Cressie. *Statistics for Spatial Data*. Wiley, 1993.
- Noel Cressie and Christopher K Wikle. *Statistics for spatio-temporal data*. John Wiley & Sons, 2015.
- David B Dahl, Devin J Johnson, and Peter Müller. Search algorithms and loss functions for bayesian clustering. *Journal of Computational and Graphical Statistics*, 31(4):1189–1201, 2022.
- Pierre Deville, Catherine Linard, Samuel Martin, Marius Gilbert, Forrest R Stevens, Andrea E Gaughan, Vincent D Blondel, and Andrew J Tatem. Dynamic population mapping using mobile phone data. *Proceedings of the National Academy of Sciences*, 111(45):15888–15893, 2014.
- T Goicoa, A Adin, MD Ugarte, and JS Hodges. In spatio-temporal disease mapping models, identifiability constraints affect pql and inla results. *Stochastic Environmental Research and Risk Assessment*, 32:749–770, 2018.
- Avril Hegarty and Daniel Barry. Bayesian disease mapping using product partition models. *Statistics in medicine*, 27(19):3868–3893, 2008.
- Mark S Kaiser and Noel Cressie. The construction of multivariate distributions from markov random fields. *Journal of Multivariate Analysis*, 73(2):199–220, 2000.
- Leonhard Knorr-Held and Günter Raßer. Bayesian detection of clusters and discontinuities in disease maps. *Biometrics*, 56(1):13–21, 2000.
- Leonhard Knorr-Held and Håvard Rue. On block updating in markov random field models for disease mapping. *Scandinavian Journal of Statistics*, 29(4):597–614, 2002. ISSN 03036898, 14679469. URL <http://www.jstor.org/stable/4616737>.

- Jane Law, Matthew Quick, and Ping Chan. Bayesian spatio-temporal modeling for analysing local patterns of crime over time at the small-area level. *Journal of quantitative criminology*, 30(1):57–78, 2014.
- Duncan Lee, Alastair Rushworth, and Gary Napier. Carbayesst: An r package for spatio-temporal areal unit modelling with conditional autoregressive priors. *R Package Version*, 2, 2015.
- Brian G. Leroux, Xingye Lei, and Norman Breslow. Estimation of disease rates in small areas: A new mixed model for spatial dependence. In M. Elizabeth Halloran and Donald Berry, editors, *Statistical Models in Epidemiology, the Environment, and Clinical Trials*, pages 179–191, New York, NY, 2000. Springer New York. ISBN 978-1-4612-1284-3.
- Guangquan Li, Robert Haining, Sylvia Richardson, and Nicky Best. Space–time variability in burglary risk: a bayesian spatio-temporal modelling approach. *Spatial Statistics*, 9: 180–191, 2014.
- Yu Liu, Xi Liu, Song Gao, Li Gong, Chaogui Kang, Ye Zhi, Guanghai Chi, and Li Shi. Social sensing: A new approach to understanding our socioeconomic environments. *Annals of the Association of American Geographers*, 105(3):512–530, 2015.
- Fabio Manfredini, Paola Pucci, Piercesare Secchi, Paolo Tagliolato, Simone Vantini, and Valeria Vitelli. Treelet decomposition of mobile phone data for deriving city usage and mobility pattern in the milan urban region. In *Advances in complex data modeling and computational methods in statistics*, pages 133–147. Springer, 2015.
- Peter Müller, Fernando Quintana, and Gary L Rosner. A product partition model with regression on covariates. *Journal of Computational and Graphical Statistics*, 20(1):260–278, 2011.
- R.M. Neal. Markov chain sampling methods for dirichlet process mixture models. *Journal of Computational and Graphical Statistics*, 9:249–265, 2000.

- Garritt L Page and Fernando A Quintana. Spatial product partition models. *Bayesian Analysis*, 11(1):265–298, 2016.
- Garritt L Page, Fernando A Quintana, and David B Dahl. Dependent modeling of temporal sequences of random partitions. *Journal of Computational and Graphical Statistics*, 31(2):614–627, 2022.
- Fernando A Quintana and Pilar L Iglesias. Bayesian clustering and product partition models. *Journal of the Royal Statistical Society: Series B (Statistical Methodology)*, 65(2):557–574, 2003.
- Tuomas Rajala, Petteri Packalen, Mari Myllymäki, and Annika Kangas. Improving detection of changepoints in short and noisy time series with local correlations: Connecting the events in pixel neighbourhoods. *Journal of Agricultural, Biological and Environmental Statistics*, pages 1–27, 2023.
- William M. Rand. Objective criteria for the evaluation of clustering methods. *Journal of the American Statistical Association*, 66(336):846–850, 1971. doi: 10.1080/01621459.1971.10482356.
- Havard Rue and Leonhard Held. *Gaussian Markov Random Fields: Theory And Applications (Monographs on Statistics and Applied Probability)*. Chapman & Hall/CRC, 2005. ISBN 1584884320.
- Håvard Rue, Sara Martino, and Nicolas Chopin. Approximate bayesian inference for latent gaussian models by using integrated nested laplace approximations. *Journal of the Royal Statistical Society Series B*, 71:319–392, 04 2009.
- Piercesare Secchi, Simone Vantini, and Valeria Vitelli. Analysis of spatio-temporal mobile phone data: a case study in the metropolitan area of Milan. *Statistical Methods & Applications*, 24(2):279–300, jul 2015. ISSN 1618-2510. doi: 10.1007/s10260-014-0294-3. URL <http://link.springer.com/10.1007/s10260-014-0294-3>.

- Chaoming Song, Zehui Qu, Nicholas Blumm, and Albert-László Barabási. Limits of predictability in human mobility. *Science*, 327(5968):1018–1021, 2010.
- Patrizia Sulis, Ed Manley, Chen Zhong, and Michael Batty. Using mobility data as proxy for measuring urban vitality. *Journal of Spatial Information Science*, 16:137–162, 2018.
- Wei Tu, Tingting Zhu, Jizhe Xia, Yulun Zhou, Yani Lai, Jincheng Jiang, and Qingquan Li. Portraying the spatial dynamics of urban vibrancy using multisource urban big data. *Computers, Environment and Urban Systems*, 80:101428, 2020.
- S. Wade and Z. Ghahramani. Bayesian Cluster Analysis: Point Estimation and Credible Balls (with Discussion). *Bayesian Anal.*, 13(2):559 – 626, 2018.
- Jonathan Wakefield and Albert Kim. A bayesian model for cluster detection. *Biostatistics*, 14(4):752–765, 2013.
- Zhensheng Wang, Yang Yue, Biao He, Ke Nie, Wei Tu, Qingyun Du, and Qingquan Li. A bayesian spatio-temporal model to analyzing the stability of patterns of population distribution in an urban space using mobile phone data. *International Journal of Geographical Information Science*, 35(1):116–134, 2021.
- Claudia Wehrhahn, Samuel Leonard, Abel Rodriguez, and Tatiana Xifara. A bayesian approach to disease clustering using restricted chinese restaurant processes. *Electronic Journal of Statistics*, 14(1):1449–1478, 2020.

A MCMC algorithm

To obtain posterior samples from the joint distribution of the parameters, $\pi(\boldsymbol{\phi}|\mathbf{y}^{obs})$, here we describe the full-conditional distributions of the Metropolis-within-Gibbs sampler algorithm for all blocks of parameters in $\boldsymbol{\phi} = (\mathbf{y}^{mis}, \boldsymbol{\beta}, \boldsymbol{\rho}, \mathbf{s}, \bar{t}, \mathbf{u}, (\tau_1^2, \dots, \tau_{n_R}^2), (\sigma_{\epsilon_1}^2, \dots, \sigma_{\epsilon_{n_R}}^2), \boldsymbol{\mu}_\beta, \boldsymbol{\Sigma}_\beta)$, where $\boldsymbol{\rho} = (\rho_1, \dots, \rho_{n_R})$, $\mathbf{s} = (\mathbf{s}^1, \dots, \mathbf{s}^{n_R})$ and $\bar{t} = (\bar{t}_0, \dots, \bar{t}_M)$.

1. update \mathbf{y}^{mis} : for i and t such that the observation is missing:

$$y_{it}^{mis} | \mathbf{y}^{obs}, r_t, s_i^{r_t}, \boldsymbol{\beta}_{s_i^{r_t} r_t} \sim N(\mathbf{x}'_t \boldsymbol{\beta}_{s_i^{r_t} r_t} + u_{ir}, \sigma_{\epsilon_r}^2)$$

2. update $\boldsymbol{\beta}_r^*$, for $r = 1, \dots, n_R$. For each $j = 1, \dots, K_r$, sample from:

$$\begin{aligned} p(\boldsymbol{\beta}_{j_r}^* | \mathbf{y}, \boldsymbol{\phi}) &\propto N_K(\boldsymbol{\mu}_{\beta_r}, \boldsymbol{\Sigma}_{\beta_r}) \prod_{t:r_t=r} \prod_{i \in C_j^{r_t}} N(y_{it} | \mathbf{x}'_t \boldsymbol{\beta}_{s_i^{r_t} r}^* + u_{ir}, \sigma_{\epsilon_r}^2) \\ &\propto \exp\left\{-\frac{1}{2}(\boldsymbol{\beta}_{j_r}^* - \boldsymbol{\mu}_{\beta_r})' \boldsymbol{\Sigma}_{\beta_r}^{-1} (\boldsymbol{\beta}_{j_r}^* - \boldsymbol{\mu}_{\beta_r}) - \frac{1}{2\sigma_{\epsilon_r}^2} \sum_{t:r_t=r} \sum_{i \in C_j^{r_t}} (y_{it} - \mathbf{x}'_t \boldsymbol{\beta}_{j_r}^* - u_{ir})^2\right\} \end{aligned}$$

yielding $\boldsymbol{\beta}_{j_r}^* | \mathbf{y}, \boldsymbol{\phi} \sim N_K(\mathbf{m}_{\beta_{j_r}^*}, \mathbf{S}_{\beta_{j_r}^*})$, where

$$\begin{aligned} \mathbf{S}_{\beta_{j_r}^*} &= \left(\boldsymbol{\Sigma}_{\beta_r}^{-1} + \frac{n_j^r}{\sigma_{\epsilon_r}^2} \sum_{t:r_t=r} \mathbf{x}_t \mathbf{x}'_t \right)^{-1} \\ \mathbf{m}_{\beta_{j_r}^*} &= \left(\boldsymbol{\Sigma}_{\beta_r}^{-1} \boldsymbol{\mu}_{\beta_r} + \sum_{t:r_t=r} \sum_{i \in C_j^{r_t}} \mathbf{x}_t \frac{(y_{it} - u_{ir})}{\sigma_{\epsilon_r}^2} \right) \mathbf{S}_{\beta_{j_r}^*} \end{aligned}$$

3. update $\boldsymbol{\mu}_{\beta_r}, \boldsymbol{\Sigma}_{\beta_r}$, for $r = 1, \dots, n_R$. We impose a diagonal structure on the covariance matrix, such that $\boldsymbol{\Sigma}_{\beta_r} = \text{diag}_K(\sigma_{\beta_{r,1}}^2, \dots, \sigma_{\beta_{r,K}}^2)$. Thus, the joint prior distribution is:

$$p(\boldsymbol{\mu}_{\beta_r}, \boldsymbol{\Sigma}_{\beta_r}) = N_K(\mathbf{m}_{\boldsymbol{\mu}_{\beta_r}}, \text{diag}_K(\sigma_{\beta_{r,1}}^2, \dots, \sigma_{\beta_{r,K}}^2)) \prod_{l=1}^K \text{inv-Gamma}(a_{\boldsymbol{\Sigma}_{\beta_r}}, b_{\boldsymbol{\Sigma}_{\beta_r}})$$

and the full conditionals are:

$$\sigma_{\beta_r, l}^2 | \mathbf{y}, \phi \sim \text{inv-Gamma} \left(a_{\sigma_{\beta_r}^2} + \frac{1 + K_r}{2}, b_{\sigma_{\beta_r}^2} + \frac{(\boldsymbol{\mu}_{\beta_r, l} - \mathbf{m}_{\beta_r, l})^2}{2} + \frac{\sum_{j=1}^{K_r} (\boldsymbol{\beta}_{jrl}^* - \boldsymbol{\mu}_{\beta_r, l})^2}{2} \right)$$

$$l = 1, \dots, K,$$

$$\boldsymbol{\mu}_{\beta_r} | \mathbf{y}, \phi \sim \text{N}_K \left(\frac{\mathbf{m}_{\boldsymbol{\mu}_{\beta_r}} + \sum_{j=1}^{K_r} \boldsymbol{\beta}_{jr}^*}{1 + K_r}, \frac{\text{diag}_K(\sigma_{\beta_r, 1}^2, \dots, \sigma_{\beta_r, K}^2)}{1 + K_r} \right)$$

4. (i) update s^r , for $r = 1, \dots, n_R$. For each $i = 1, \dots, I$, sample from:

$$P(s_i^r = j | \mathbf{y}^{-i}, \mathbf{s}_{-i}^r, \rho_r^{-i}, \boldsymbol{\beta}_r^*, r, u_{ir}, \sigma_{\epsilon_r}^2, \kappa, \xi) \propto \begin{cases} n_j^{-i} e^{-\xi \ell^j(\{i\})} \prod_{t: r_t=r} \text{N}(y_{it} | \mathbf{x}'_t \boldsymbol{\beta}_{jr}^* + u_{ir}, \sigma_{\epsilon_r}^2), & j = 1, \dots, K_r^{-i} \\ \kappa e^{-\xi \ell^j(\{i\})} \int_{\mathbb{R}^K} \prod_{t: r_t=r} \text{N}(y_{it} | \mathbf{x}'_t \boldsymbol{\beta} + u_{ir}, \sigma_{\epsilon_r}^2) P_0(\boldsymbol{\beta}) d\boldsymbol{\beta}, & j = K_r^{-i} + 1 \end{cases}$$

The integral in the second line is the density of a multivariate normal vector $\mathbf{y}_i := (y_{it}, r_t = r)$; we denote by m_r its length, and by \mathbf{x}_r the matrix with rows given by $(\mathbf{x}'_t, r_t = r)$. It is straightforward to prove that the mean of this density is

$$\mathbb{E}(\mathbf{Y}_i) = \mathbb{E}[\mathbb{E}(\mathbf{Y}_i | \boldsymbol{\beta})] = \mathbb{E}[\mathbf{x}_r \boldsymbol{\beta}] + u_{ir} \mathbf{1} = \mathbf{x}_r \boldsymbol{\mu}_{\boldsymbol{\beta}} + u_{ir} \mathbf{1},$$

here $\mathbf{1}$ is the vector of ones (of the same length as \mathbf{y}_i). Similarly we prove that the covariance matrix of \mathbf{Y}_i is such that

$$\text{Cov}(\mathbf{Y}_i) = \text{Cov}(\mathbb{E}(\mathbf{Y}_i | \boldsymbol{\beta})) + \mathbb{E}(\text{Cov}(\mathbf{Y}_i | \boldsymbol{\beta})) = \text{Cov}(\mathbf{x}_r \boldsymbol{\beta} + u_{ir} \mathbf{1}) + \mathbb{E}(\sigma_{\epsilon_r}^2 \mathbb{I}_{m_r}) = \mathbf{x}_r \boldsymbol{\Sigma}_{\boldsymbol{\beta}} \mathbf{x}_r' + \sigma_{\epsilon_r}^2 \mathbb{I}_{m_r}$$

In case a new cluster $K_r^{-i} + 1$ is formed, a new value of the vector $\boldsymbol{\beta}_{K_r^{-i}+1, r}^*$ has to be sampled from the distribution in sampling step 2 for the data vector \mathbf{y}_i with respect to all harmonic covariates \mathbf{x}_t and $t : r_t = r$ and $n_{K_r^{-i}+1}^r = 1$.

(ii) An alternative Pólya urn algorithm to the one described above can be used to mitigate the problems arising in high dimensional settings. Following [Neal, 2000] we implement the Algorithm 2, marginalising over the values of the coefficients $\tilde{\beta}_{j_r}^*$ in the first line above, and the allocation probabilities become:

$$P(s_i^r = j | \mathbf{y}^{-i}, \mathbf{s}_{-i}^r, \rho_r^{-i}, \boldsymbol{\beta}_r^*, r, u_{ir}, \sigma_{\epsilon_r}^2, \kappa, \xi) \propto \begin{cases} n_j^{-i} e^{-\xi \ell^j(\{i\})} \int_{\mathbb{R}^{2p}} \prod_{t:r_t=r} \mathbf{N}(y_{it} | \mathbf{x}'_t \boldsymbol{\beta}_{j_r}^* + u_{ir}, \sigma_{\epsilon_r}^2) \mathbf{N}_K(\boldsymbol{\beta}_{j_r}^* | \mathbf{m}_{\boldsymbol{\beta}_{j_r}^*}, \mathbf{S}_{\boldsymbol{\beta}_{j_r}^*}) d\boldsymbol{\beta}_{j_r}^*, & j = 1, \dots, K_r^{-i}, \\ \kappa e^{-\xi \ell^j(\{i\})} \int_{\mathbb{R}^K} \prod_{t:r_t=r} \mathbf{N}(y_{it} | \mathbf{x}'_t \boldsymbol{\beta} + u_{ir}, \sigma_{\epsilon_r}^2) P_0(\boldsymbol{\beta}) d\boldsymbol{\beta}, & j = K_r^{-i} + 1; \end{cases}$$

where the mean and covariance matrix $\mathbf{m}_{\boldsymbol{\beta}_{j_r}^*}$ and $\mathbf{S}_{\boldsymbol{\beta}_{j_r}^*}$ are computed as in point (2), considering all areal units in the j -th cluster after removing the i -th areal unit, for $j = 1, \dots, K_r^{-i}$. The computation of the integral in the second line are analogous to the ones of point 4(i), while a similar technique can be used to compute the integral in the first line, obtaining as marginal distribution for the vector \mathbf{Y}_i a multivariate Gaussian with mean and covariance equal to:

$$\mathbb{E}(\mathbf{Y}_i) = \mathbb{E}[\mathbb{E}(\mathbf{Y}_i | \boldsymbol{\beta})] = \mathbb{E}[\mathbf{x}_r \boldsymbol{\beta}_{j_r}^*] + u_{ir} \mathbf{1} = \mathbf{x}_r \mathbf{m}_{\boldsymbol{\beta}_{j_r}^*} + u_{ir} \mathbf{1},$$

$$\text{Cov}(\mathbf{Y}_i) = \text{Cov}(\mathbb{E}(\mathbf{Y}_i | \boldsymbol{\beta})) + \mathbb{E}(\text{Cov}(\mathbf{Y}_i | \boldsymbol{\beta})) = \text{Cov}(\mathbf{x}_r \boldsymbol{\beta}_{j_r}^* + u_{ir} \mathbf{1}) + \mathbb{E}(\sigma_{\epsilon}^2 \mathbb{I}_{m_r}) = \mathbf{x}_r \mathbf{S}_{\boldsymbol{\beta}_{j_r}^*} \mathbf{x}_r' + \sigma_{\epsilon}^2 \mathbb{I}_{m_r}$$

5. update $\mathbf{u}_r = (u_{1r}, \dots, u_{I_r})$, for $r = 1, \dots, n_R$ by sampling:

$$\begin{aligned} p(\mathbf{u}_r | \mathbf{y}, \phi) &= \mathbf{N}_I(\mathbf{u}_r | \mathbf{m}_{\mathbf{u}_r}, \mathbf{S}_{\mathbf{u}_r}) \\ \mathbf{S}_{\mathbf{u}_r} &= \left(\frac{Q(\zeta_r, W)}{\tau_r^2} + \frac{m_r}{\sigma_{\epsilon_r}^2} \mathbb{I}_I \right)^{-1} \\ \mathbf{m}_{\mathbf{u}_r} &= \mathbf{S}_{\mathbf{u}_r} \left(\frac{Q(\zeta_r, W)}{\tau_r^2} \boldsymbol{\mu}_u + \frac{1}{\sigma_{\epsilon_r}^2} \sum_{t:r_t=r} (\mathbf{y}_t - \mathbf{x}'_t \boldsymbol{\beta}_{s^r}^*) \right) \end{aligned}$$

where m_r is the size of $\{t : r_t = r\}$, and will depend on the change-points.

6. because $\tau_r^2 \sim \text{inv-Gamma}(a_{\tau_r^2}, b_{\tau_r^2})$, then:

$$\tau_r^2 | \mathbf{y}, \phi \sim \text{inv-Gamma} \left(a_{\tau_r^2} + \frac{I}{2}, b_{\tau_r^2} + \frac{1}{2} \mathbf{u}'_r Q(\zeta_r, W) \mathbf{u}_r \right)$$

7. update $\sigma_{\epsilon_r}^2$, by sampling:

$$p(\sigma_{\epsilon_r}^2 | \mathbf{y}, \phi) = \text{inv-Gamma} \left(\sigma_{\epsilon_r}^2 \left| a_{\sigma_{\epsilon_r}^2} + \frac{IT}{2}, b_{\sigma_{\epsilon_r}^2} + \frac{1}{2} \sum_{t=1}^T \sum_{i=1}^I (y_{it} - \mathbf{x}'_t \boldsymbol{\beta}_{it} - u_{it})^2 \right. \right)$$

8. update \bar{t}_m , for $m = 1, \dots, M - 1$ from the full conditional proportional to:

$$p(\bar{t}_m | \mathbf{y}, \phi) \propto \mathbb{I}_{\{\lambda_m - n_\lambda, \dots, \lambda_m + n_\lambda\}}(\bar{t}_m) \left[\prod_{j_1 \in \{\lambda_m - n_\lambda, \dots, \bar{t}_m\}} \prod_{i=1}^I \text{N}(y_{ij_1} | \mathbf{x}'_{j_1} \boldsymbol{\beta}_{s_i^{r_1}}^* + u_{ir_1}, \sigma_{\epsilon_{r_1}}^2) \right] \left[\prod_{j_2 \in \{\bar{t}_m + 1, \dots, \lambda_m + n_\lambda\}} \prod_{i=1}^I \text{N}(y_{ij_2} | \mathbf{x}'_{j_2} \boldsymbol{\beta}_{s_i^{r_2}}^* + u_{ir_2}, \sigma_{\epsilon_{r_2}}^2) \right]$$

where $r_1 = r_{\bar{t}_m}$ and $r_2 = r_{\bar{t}_m + 1}$. To improve the mixing of the change-points \bar{t}_m , we implement a marginalised version of the above sampling step, after integrating out the cluster-specific parameters $\boldsymbol{\beta}_{s_i^r}^*$, for $m = 1, \dots, M - 1$. This yields the following probabilities:

$$p(\bar{t}_m | \mathbf{y}, \phi) \propto \mathbb{I}_{\{\lambda_m - n_\lambda, \dots, \lambda_m + n_\lambda\}}(\bar{t}_m) \left[\prod_{j_1 \in \{\lambda_m - n_\lambda, \dots, \bar{t}_m\}} \text{N}_I(\mathbf{y}_{j_1} | \mathbf{x}'_{j_1} \boldsymbol{\mu}_\beta \mathbf{1}_I + \boldsymbol{\mu}_u, (\mathbf{x}_{j_1} \boldsymbol{\Sigma}_\beta \mathbf{x}'_{j_1} + \sigma_{\epsilon_{r_1}}^2) \mathbb{I}_I + \tau_{r_1}^2 Q^{-1}(\zeta_{r_1}, W)) \right] \left[\prod_{j_2 \in \{\bar{t}_m + 1, \dots, \lambda_m + n_\lambda\}} \text{N}_I(\mathbf{y}_{j_2} | \mathbf{x}'_{j_2} \boldsymbol{\mu}_\beta \mathbf{1}_I + \boldsymbol{\mu}_u, (\mathbf{x}_{j_2} \boldsymbol{\Sigma}_\beta \mathbf{x}'_{j_2} + \sigma_{\epsilon_{r_2}}^2) \mathbb{I}_I + \tau_{r_2}^2 Q^{-1}(\zeta_{r_2}, W)) \right]$$

where $\mathbf{1}_I$ is the vector of ones of length I and \mathbb{I}_I is the I -dimensional identity matrix. \mathbf{y}_j indicates the column vector of areal observations at time j .

Notice how the regime indicators are constant within each product term, clarifying the regime switch induced by the change-point \bar{t}_m , for $m = 1, \dots, M - 1$.

B APPENDIX B: simulation studies

In all the simulations, we run MCMC draws from the corresponding Gibbs sampler for 15,000 iterations, of which the first 13,000 are then discarded as burn-in, and the last 2,000 are thinned to obtain a sample of 1,000 to be used in the posterior inference. Section 3.4 in the manuscript reports a summary of the simulation experiments detailed here.

Single regime with contaminated clusters and no missing data

With the aim of testing the performance of the algorithm described in Appendix A, we set-up a simulation example characterized by only one regime ($n_R = 1$). A grid of size 12×10 is used ($I = 120$), with the clustering structure shown in Figure 11(a). The partition of the areal units used to simulate the data is composed of three clusters, two of which contaminate each other symmetrically. The aim of this simulation study is to show how the areal information included in the cohesion function in (5) can help recover the clustering structure. For each areal unit, a time series $\{y_{it}, t = 1, \dots, T\}$ of length $T = 100$ is generated from (9). We include time-varying covariates $\mathbf{x}_t \stackrel{\text{ind}}{\sim} \mathbf{N}_K(t/T, 1)$ with $K = 5$. The values of the coefficients $\boldsymbol{\beta}^*$ and of the random effects \mathbf{u} are sampled from the corresponding prior distributions, i.e. $\boldsymbol{\beta}_1^*, \dots, \boldsymbol{\beta}_3^* \stackrel{\text{iid}}{\sim} P_0(\mathbf{0}, 2.5\mathbb{I}_K)$ and $\mathbf{u} \sim \mathbf{N}_I(\mathbf{0}, \tau^2 Q(\zeta, W)^{-1})$. Additionally, we set $\tau^2 = 1$, $\sigma_\epsilon^2 = 0.5$, and $\zeta = 0.9$. The simulated dataset is shown in Figures 11(b,c).

Simulations are run using the MCMC algorithm described in Appendix A, for different values of $\xi \in \exp(-2, -1, 0, 1)$. We fix $\kappa = 0.415$, yielding $\mathbb{E}(K_I) \approx 3$ under the DP case (i.e., when $\xi = 0$). Furthermore, we compare the proposed model with the one by Hegarty and Barry [2008].

Firstly, we show the traceplots of the posterior chains of some parameters in Figure 12. The posterior chains for the areal autocorrelation parameter ζ and of the homoscedastic error σ_ϵ^2 do not seem to be strongly affected by the choice of the parameter ξ or by the model specification. However, the traceplots for τ^2 do not seem to capture the true value used in

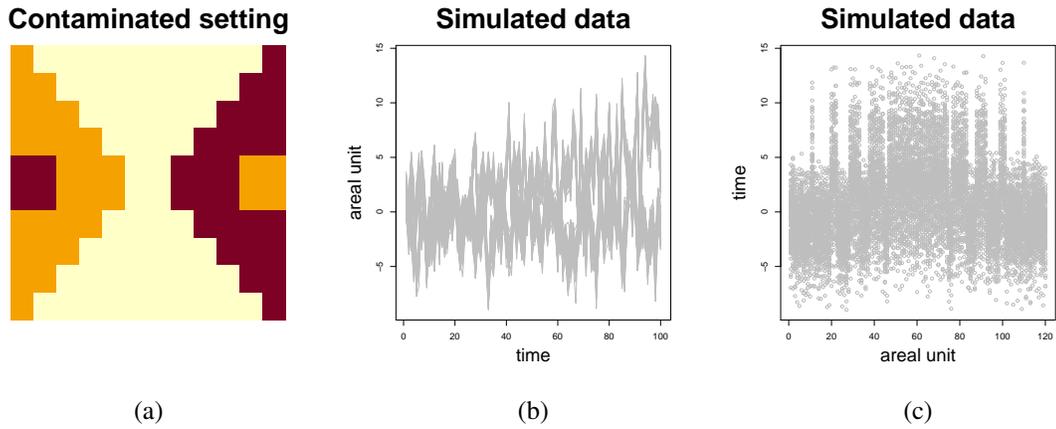


Figure 11: Simulated data ($n_R = 1$). (a) The original clustering of the data shows areal contamination. (b) Plot of the trajectories for each areal units. (c) Plot of the data for each time point as function of the areal units.

the simulations, despite convergence. This behavior seems to reflect the identifiability issues already pointed out in Section 3.4.

We proceed the investigation by looking at the posterior estimates of the partition of the areal units. We report in Figure 13 the estimates obtained by minimizing the Variation of Information loss function. Both prior choices, i.e. the proposed model and the one by Hegarty and Barry [2008], yield correct posterior estimates of the partition.

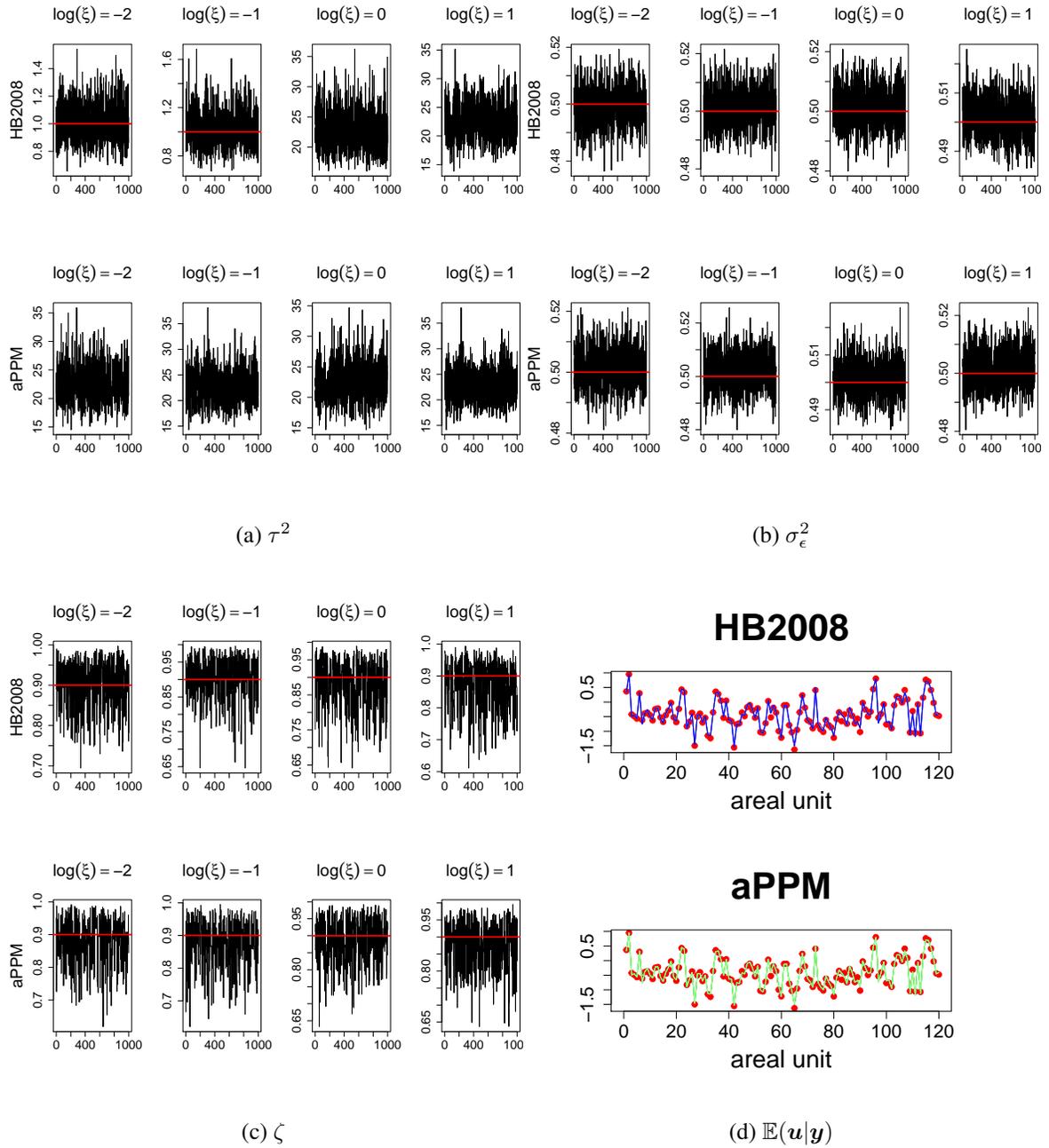


Figure 12: Simulated data ($n_R = 1$). (a,b,c) Traceplots of the parameters τ^2 , σ_ϵ^2 and ζ . The value of the parameters used to simulate the data is indicated as a red horizontal line. (d) Posterior mean of the areal random effects (truth in red).

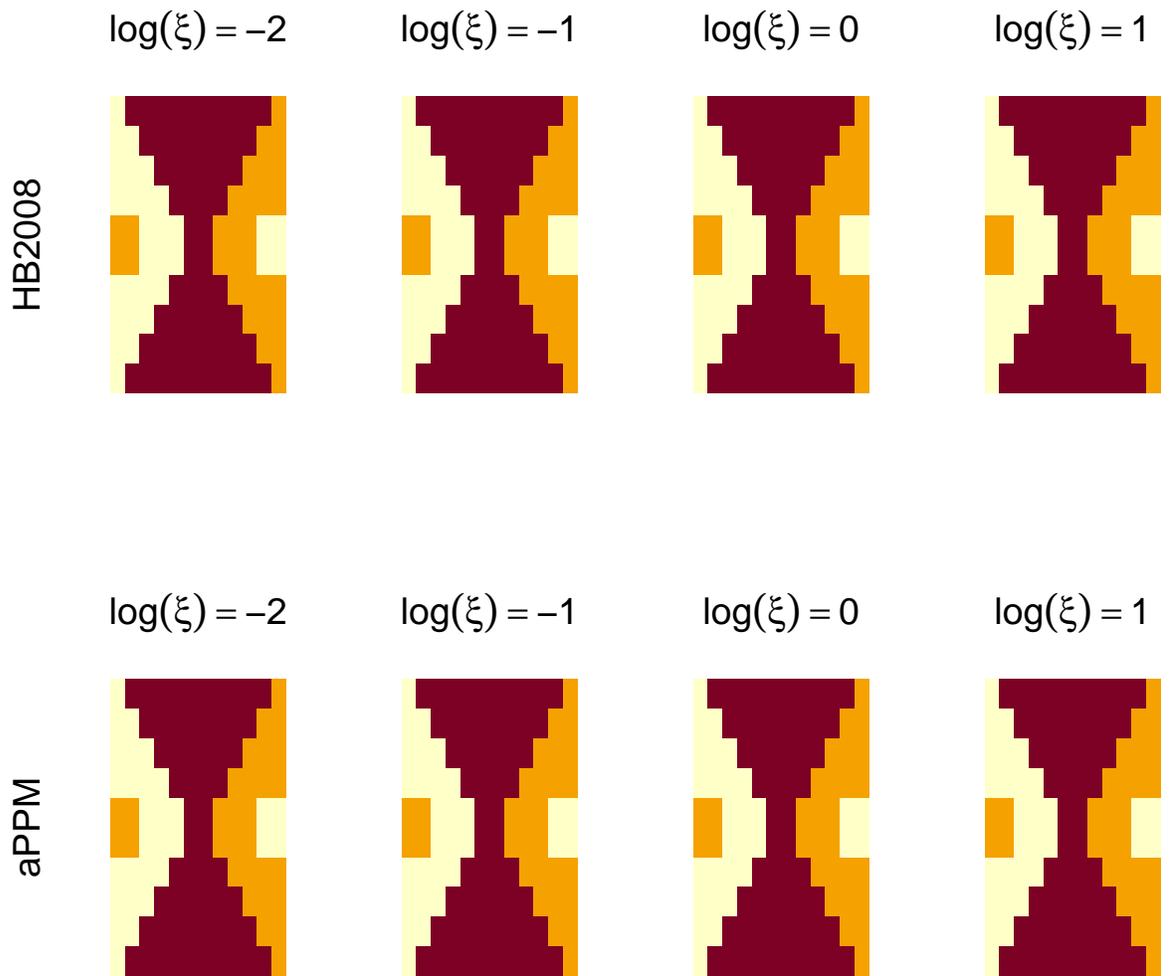


Figure 13: Simulated data ($n_R = 1$). Posterior estimates of the partition of the areal units obtained by minimizing the Variation of Information loss function.

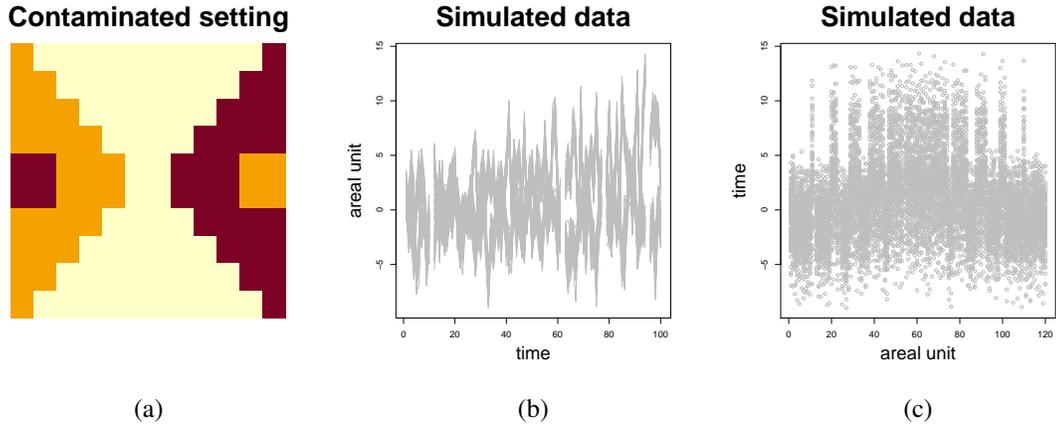


Figure 14: Simulated data ($n_R = 1$). (a) The original clustering of the data shows areal contamination. (b) Plot of the trajectories for each areal units. (c) Plot of the data for each time point as function of the areal units.

Single regime with contaminated clusters and missing data

We present another simulation example with one regime only ($n_R = 1$). As in the previous example, a grid of size 12×10 is used ($I = 120$), with similar clustering structure shown in Figure 14(a), is selected. The partition of the areal units used to simulate the data is composed of three clusters, two of which contaminate each-other symmetrically. Finally, we selected 3 areal units and 4 time points arbitrarily at random for which the whole vector of observations was considered missing, as well as 12 other points chosen uniformly at random in the areal/time space. The resulting dataset is shown in Figures 14(b,c). All the other settings are kept the same as in the previous one-regime simulation study.

Firstly, we show the traceplots of the posterior chains of some parameters in Figure 15. Similar considerations as in the previous simulations can be made for these plots. One difference lies in the posterior estimates of the variance parameter τ^2 , whose posterior distribution now is concentrated on high values for most values of ξ .

We proceed the investigation by looking at the posterior estimates of the partition of the areal units. We obtain such estimates by minimizing the Variation of Information loss func-

tion with equal costs, and are shown in Figure 16. We observe some small differences between the two posterior estimates, but they mostly agree. However, the areal units for which we have missing information throughout the whole time frame are not clustered properly, suggesting the need for a longer posterior chain and more informative prior distributions.

Finally, we report in Figures 17 and, 18, 19 the traceplots for the imputed missing values for locations missing only some time points, or the whole time series. It is clear that recovering the latter is quite challenging under all model specifications.

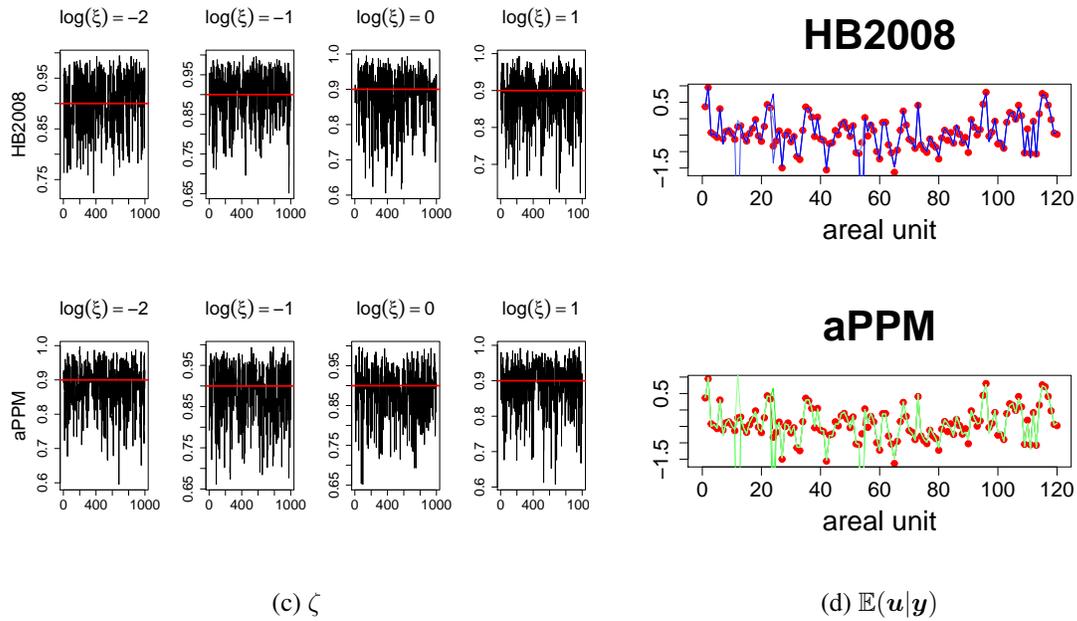
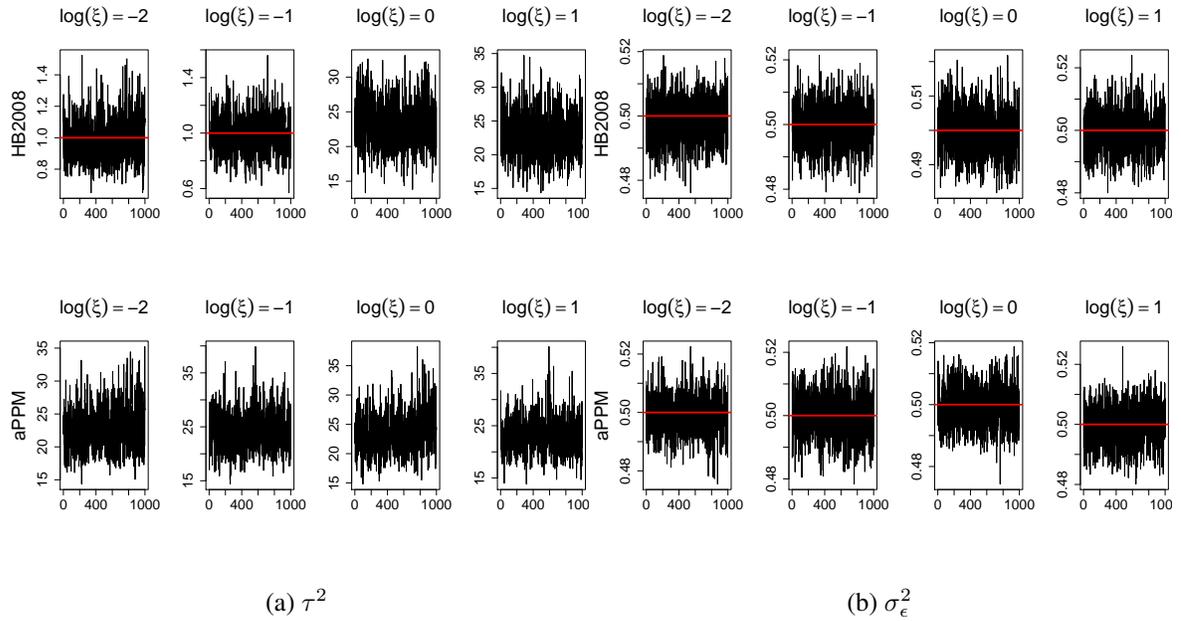


Figure 15: Simulated data ($n_R = 1$). (a,b,c) Traceplots of the parameters τ^2 , σ_ϵ^2 and ζ . The value of the parameters used to simulate the data is indicated as a red horizontal line. (d) Posterior mean of the areal random effects (truth in red).

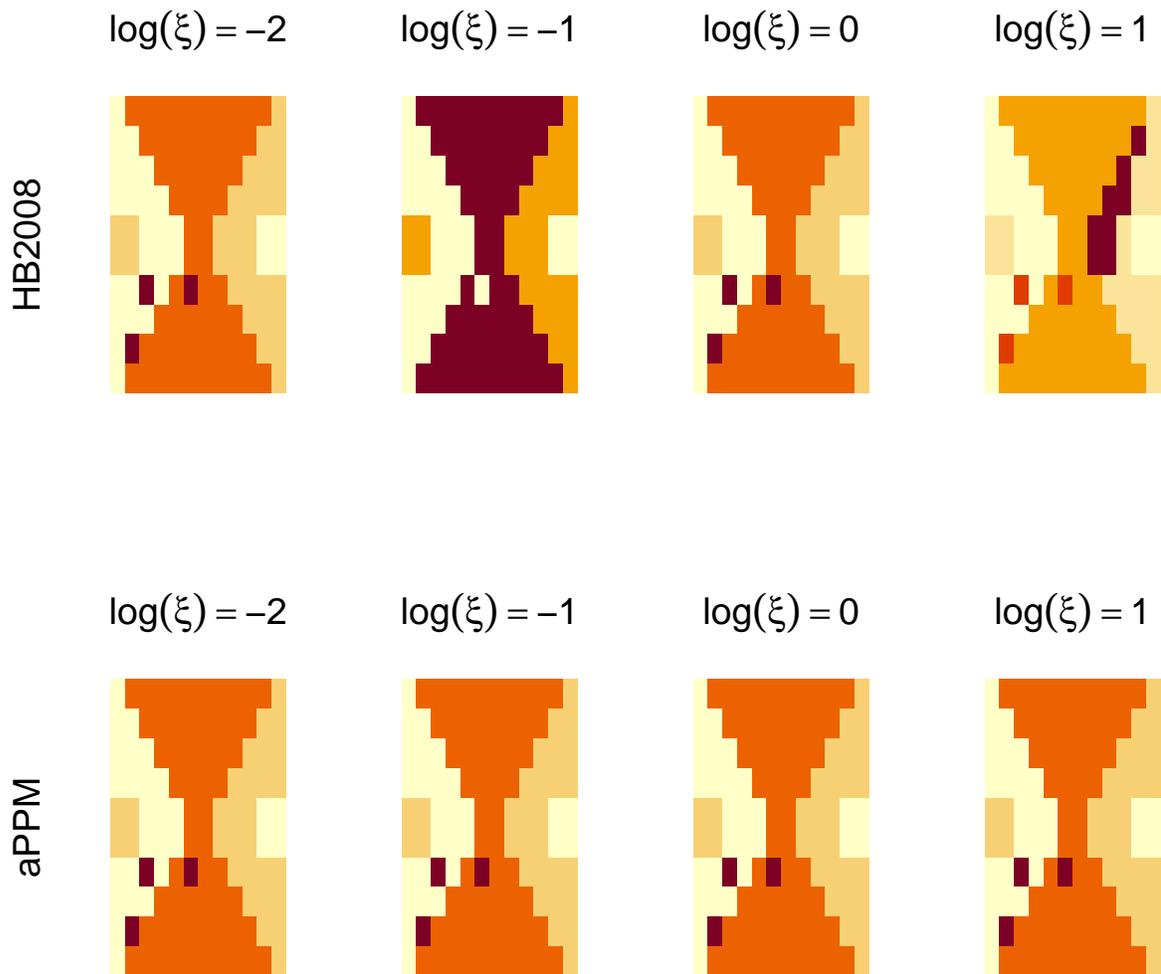


Figure 16: Simulated data ($n_R = 1$). Posterior estimates of the partition of the areal units obtained by minimizing the Variation of Information loss function.

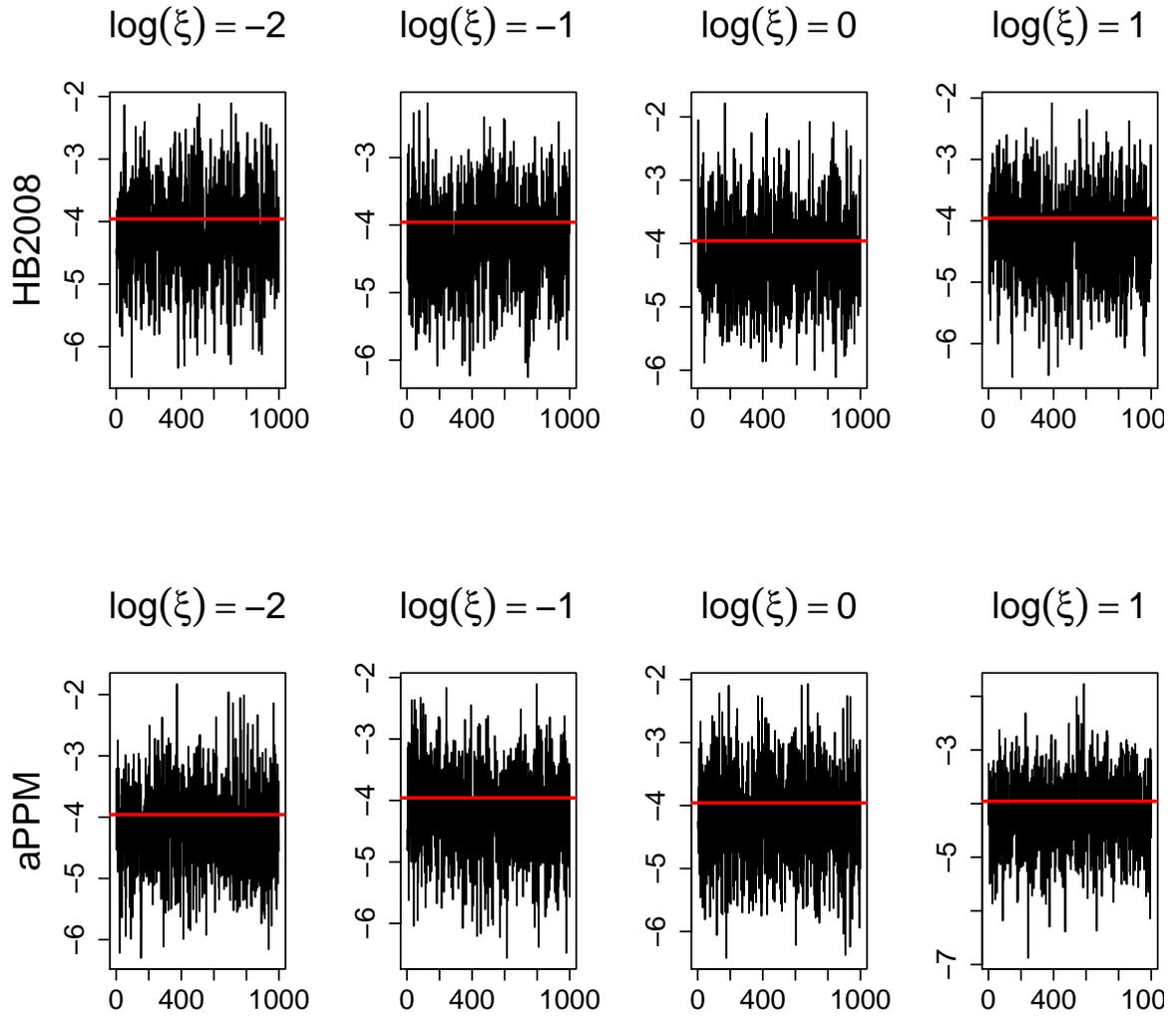


Figure 17: Simulated data ($n_R = 1$). Traceplots of the imputed missing value at location/time $(i, t) = (94, 4)$ under different model specifications.

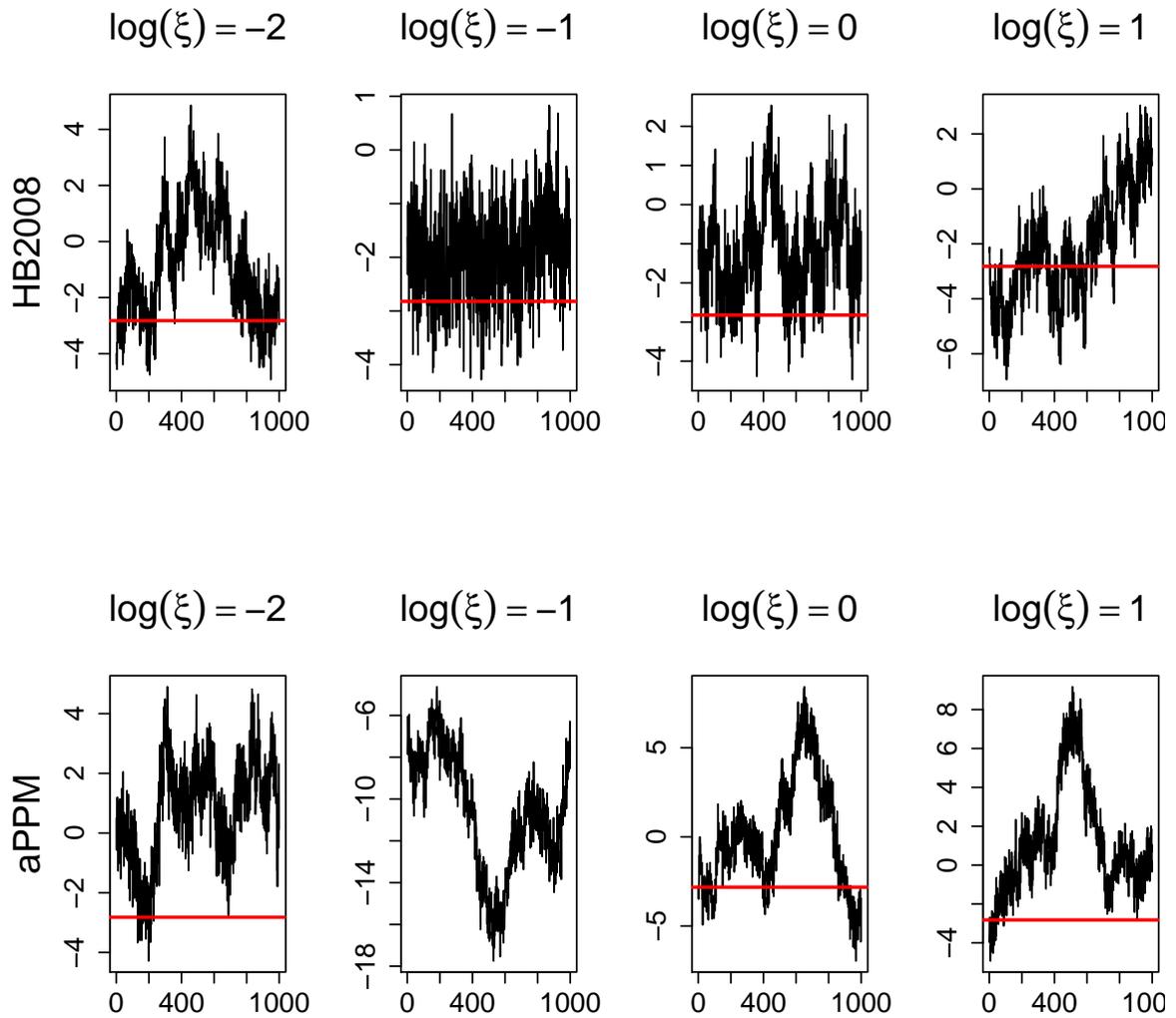


Figure 18: Simulated data ($n_R = 1$). Traceplots of the imputed missing value at location/time $(i, t) = (24, 50)$ under different model specifications. This areal unit was missing observations at all time points.

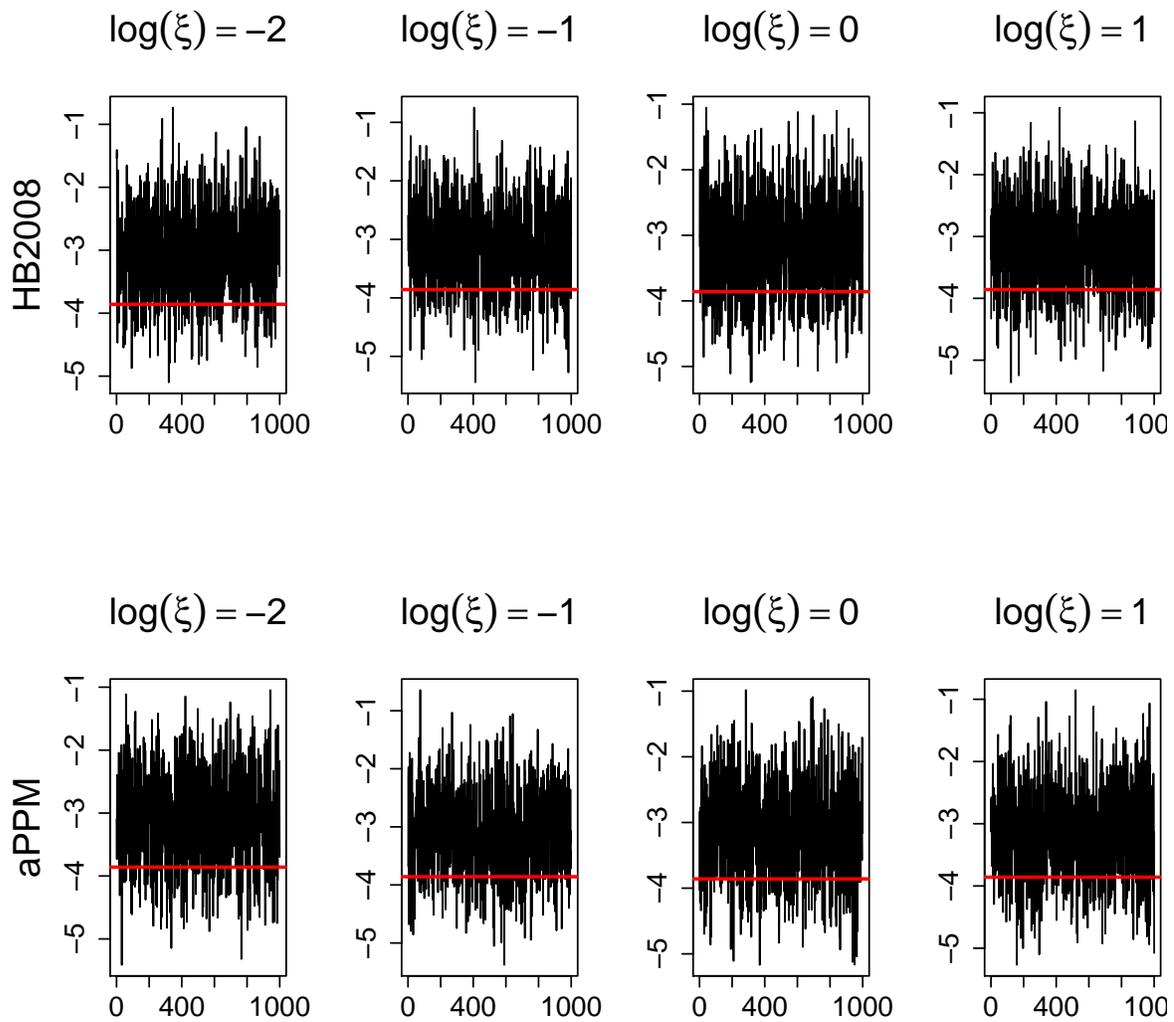


Figure 19: Simulated data ($n_R = 1$). Traceplots of the imputed missing value at location/time $(i, t) = (10, 21)$ under different model specifications. This time point was missing observations at all areal units.

Multiple regimes

We perform a simulations study presenting $n_R = 2$ regimes. Similarly to the single regime scenarios, data are simulated for a grid of size 12×10 ($I = 120$), with regime-specific clustering structure shown in Figure 20. The partition of the areal units used to simulate the data is composed of two clusters in each regime, dividing the areal units in half (regime one) or diagonally (regime 2). For each areal unit, a time series $\{y_{it}, t = 1, \dots, T\}$ of length $T = 100$ is generated from (9). We include time-varying covariates following the harmonics construction of Section 3 and select frequencies corresponding to 5, 10 and 25 time units, yielding $K = 6$. The values of the coefficients β^* and of the random effects \mathbf{u} are sampled from the corresponding prior distributions, i.e. $\beta_1^*, \dots, \beta_3^* \stackrel{\text{iid}}{\sim} P_0(\mathbf{0}, 2.5\mathbb{I}_K)$ and $\mathbf{u}_r \sim \mathbf{N}_I(\mathbf{0}, \tau_r^2 Q(\zeta_r, W)^{-1})$, for $r = 1, 2$. Additionally, we set $\tau_r^2 = 1$ and $\zeta_r = 0.75$, for $r = 1, 2$. We consider two different scenarios where the value of the variance parameter $\sigma_{\epsilon_r}^2$ is either 0.1 or 1 for both regimes. Finally, we fix the centre of the change-points to be equally spaced, i.e. $\lambda_m \in (25, 50, 75)$ and consider two different prior settings for the change-points \bar{t}_m , namely $n_\lambda \in (5, 10)$. The simulated dataset is shown in Figures 21 and 22.

Posterior inference is carried out with analogous settings as for the single regime simulations, with exception of the parameters ζ_r which are fixed to the true values 0.75, for $r = 1, 2$.

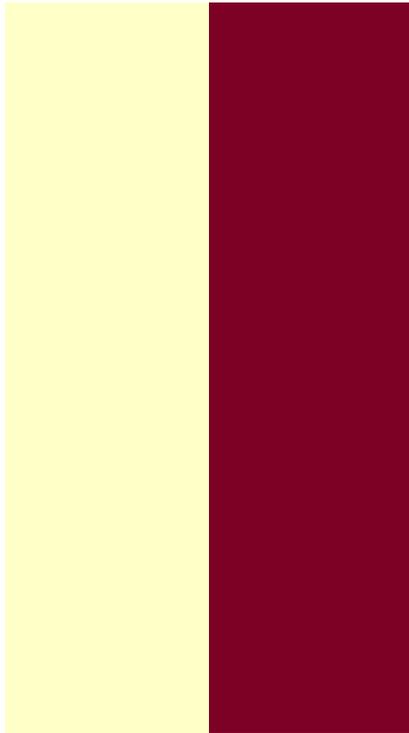
We show in Figures 23 and 24 the traceplots for the parameters τ_r^2 and $\sigma_{\epsilon_r}^2$, for $r = 1, 2$ and all scenarios considered in this simulation study. The true values of the parameters are adequately recovered in all simulation settings, although the true values are found in the tails of the posterior distributions.

We also provide posterior estimates of the underlying regime-specific partition of the areal units, obtained by minimising the Variation of Information loss function, see Figure 25.

We conclude the simulation study by presenting the posterior distribution of the change points \bar{t}_m , in Figure 26. The change-points are recovered satisfactorily, with the posterior

mode of the distribution corresponding to the values used in the simulation of the data.

regime 1



regime 2

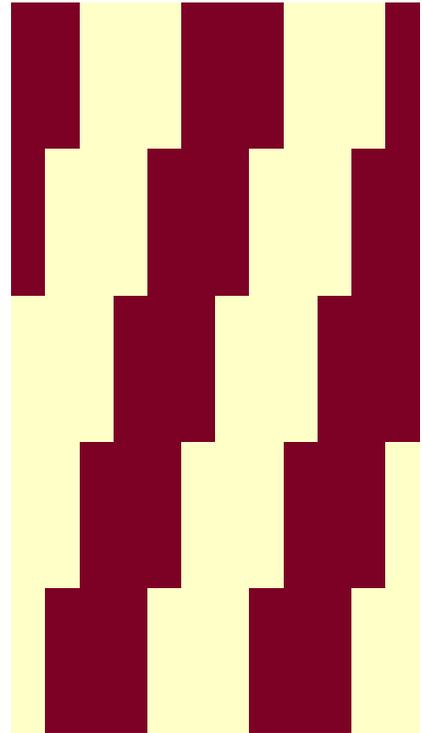
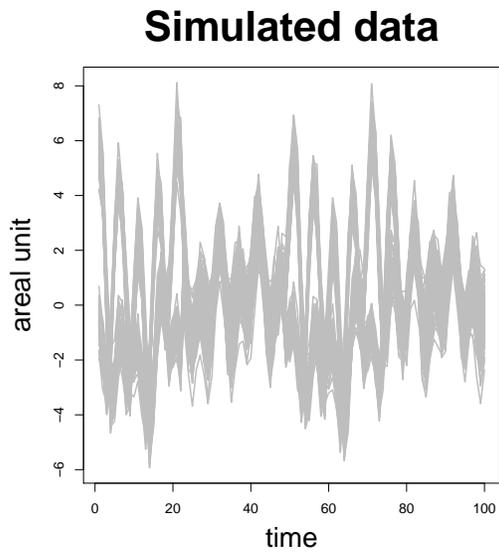
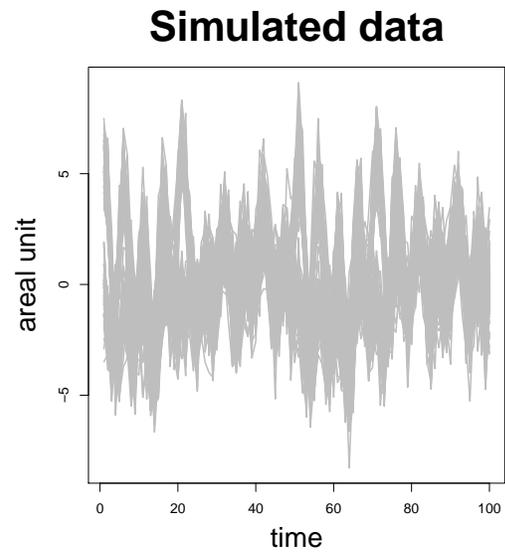


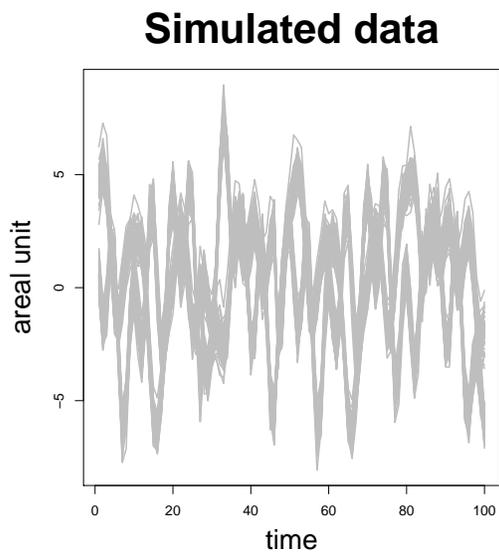
Figure 20: Simulated data ($n_R = 2$). Regime-specific partitions used to simulate the data.



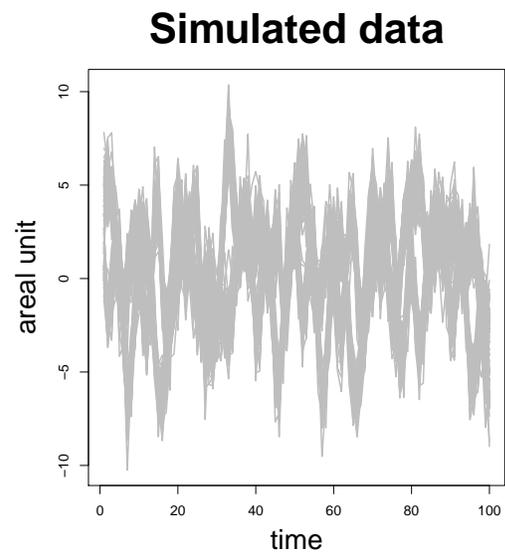
(a) $(n_\lambda, \sigma_{\epsilon_r}^2) = (5, 0.1)$



(b) $(n_\lambda, \sigma_{\epsilon_r}^2) = (5, 1)$



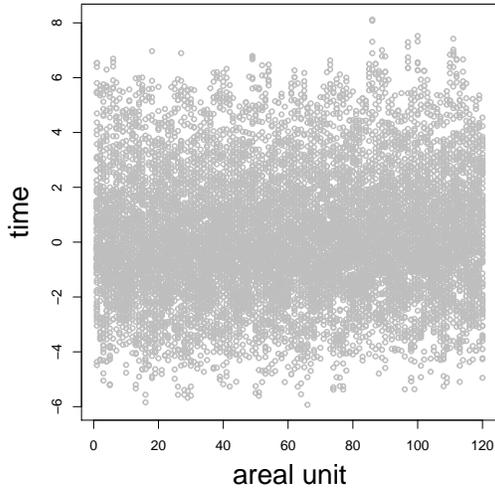
(c) $(n_\lambda, \sigma_{\epsilon_r}^2) = (10, 0.1)$



(d) $(n_\lambda, \sigma_{\epsilon_r}^2) = (10, 1)$

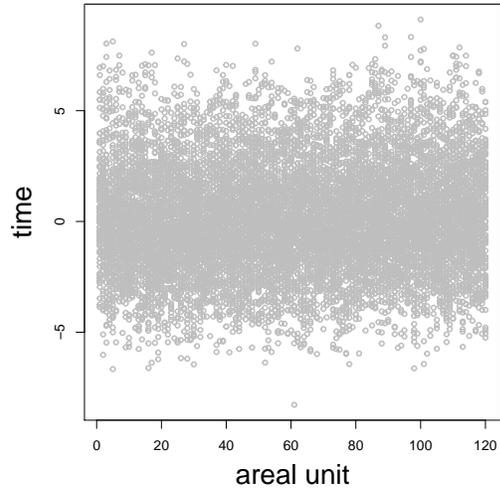
Figure 21: Simulated data ($n_R = 2$). Trajectories obtained under each simulation scenario as function of time.

Simulated data



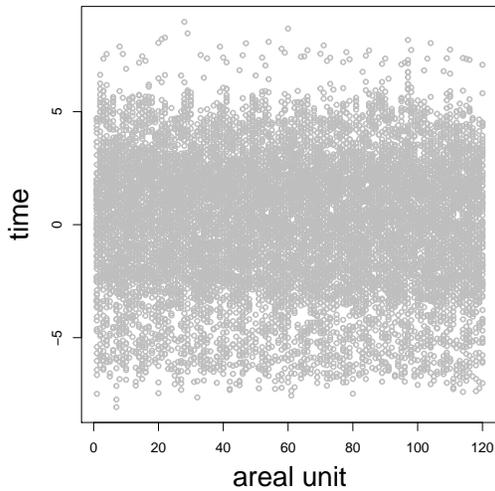
(a) $(n_\lambda, \sigma_{\epsilon_r}^2) = (5, 0.1)$

Simulated data



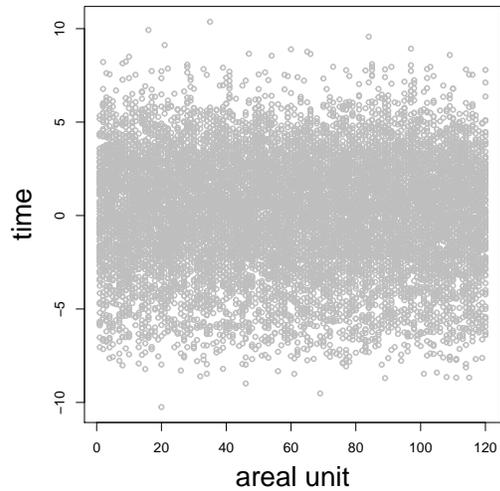
(b) $(n_\lambda, \sigma_{\epsilon_r}^2) = (5, 1)$

Simulated data



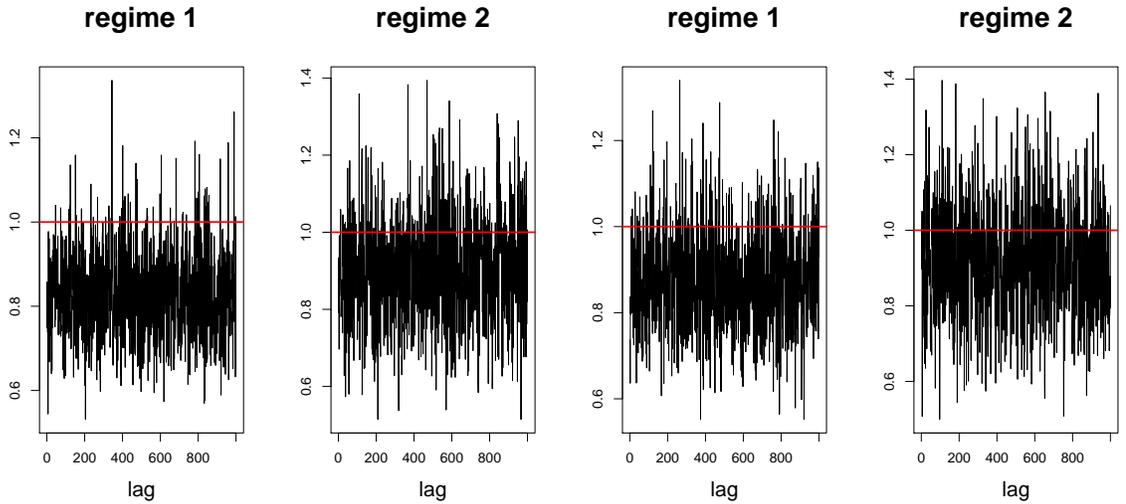
(c) $(n_\lambda, \sigma_{\epsilon_r}^2) = (10, 0.1)$

Simulated data



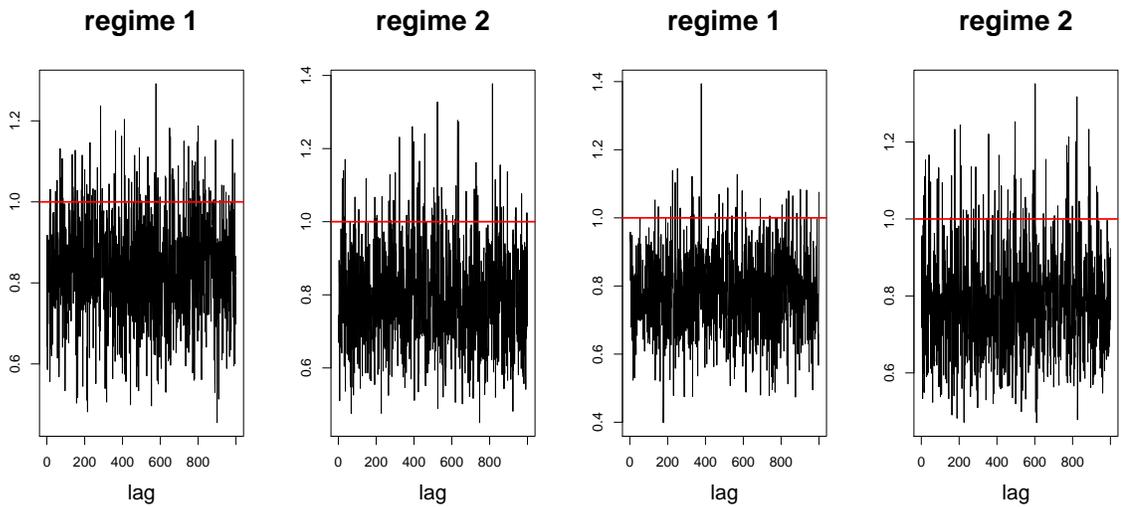
(d) $(n_\lambda, \sigma_{\epsilon_r}^2) = (10, 1)$

Figure 22: Simulated data ($n_R = 2$). Data obtained under each simulation scenario as function of the areal units.



(a) $(n_\lambda, \sigma_{\epsilon_r}^2) = (5, 0.1)$

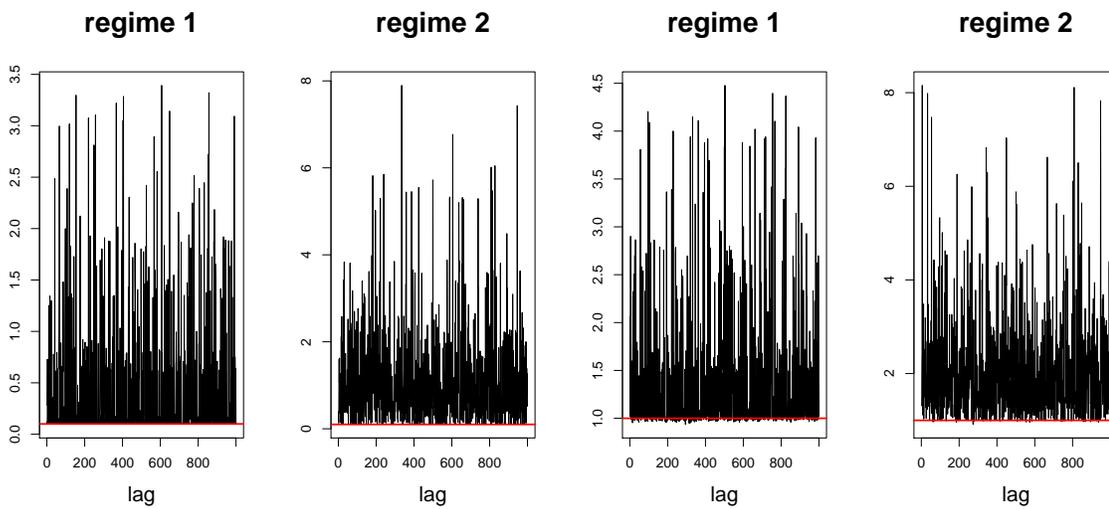
(b) $(n_\lambda, \sigma_{\epsilon_r}^2) = (5, 1)$



(c) $(n_\lambda, \sigma_{\epsilon_r}^2) = (10, 0.1)$

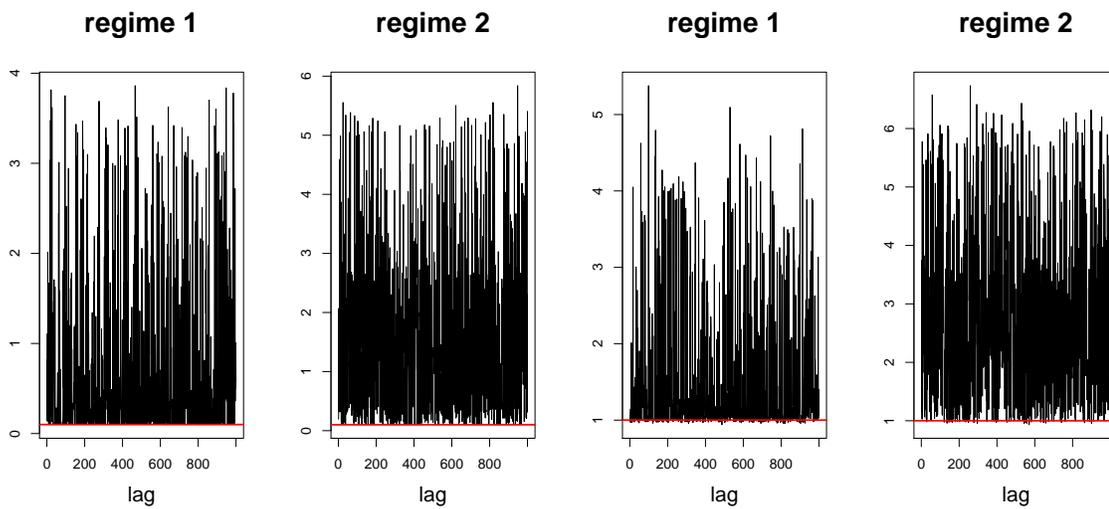
(d) $(n_\lambda, \sigma_{\epsilon_r}^2) = (10, 1)$

Figure 23: Simulated data ($n_R = 2$). Traceplots of the parameters τ_r^2 , for $r = 1, 2$. Each panel refers to a different simulation setting. The red horizontal lines in the figures indicate the true value of the parameters used for the simulations.



(a) $(n_\lambda, \sigma_{\epsilon_r}^2) = (5, 0.1)$

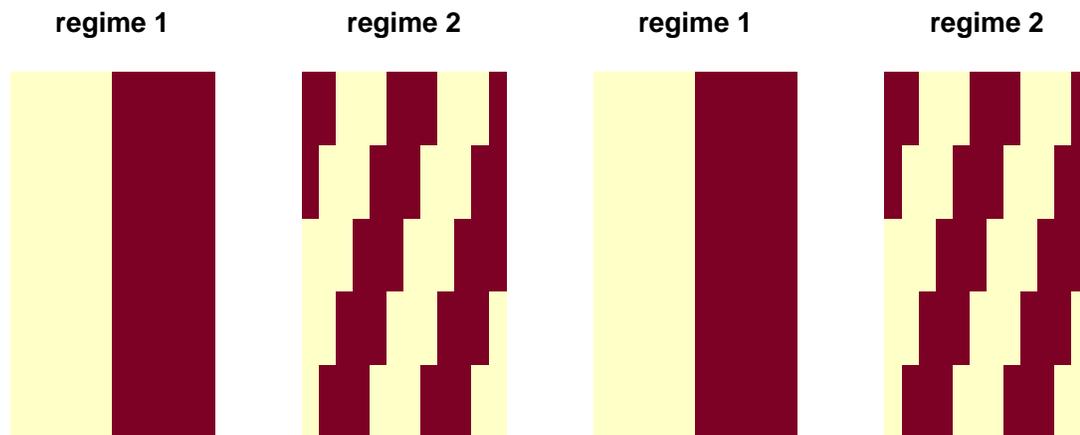
(b) $(n_\lambda, \sigma_{\epsilon_r}^2) = (5, 1)$



(c) $(n_\lambda, \sigma_{\epsilon_r}^2) = (10, 0.1)$

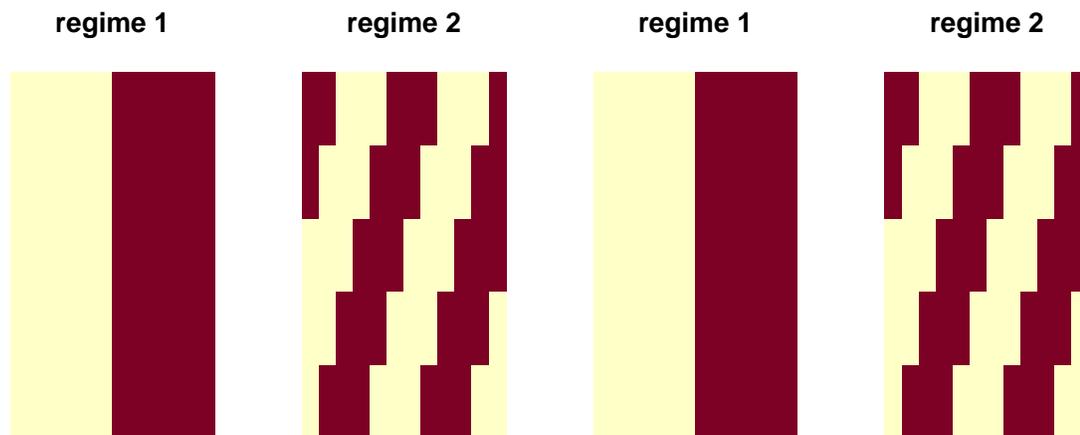
(d) $(n_\lambda, \sigma_{\epsilon_r}^2) = (10, 1)$

Figure 24: Simulated data ($n_R = 2$). Traceplots of the parameters $\sigma_{\epsilon_r}^2$, for $r = 1, 2$. Each panel refers to a different simulation setting. The red horizontal lines in the figures indicate the true value of the parameters used for the simulations.



(a) $(n_\lambda, \sigma_{\epsilon_r}^2) = (5, 0.1)$

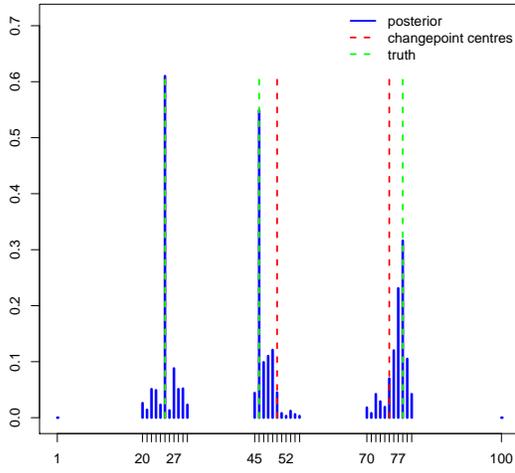
(b) $(n_\lambda, \sigma_{\epsilon_r}^2) = (5, 1)$



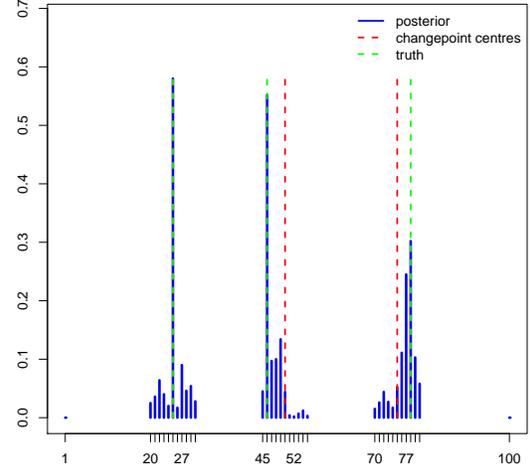
(c) $(n_\lambda, \sigma_{\epsilon_r}^2) = (10, 0.1)$

(d) $(n_\lambda, \sigma_{\epsilon_r}^2) = (10, 1)$

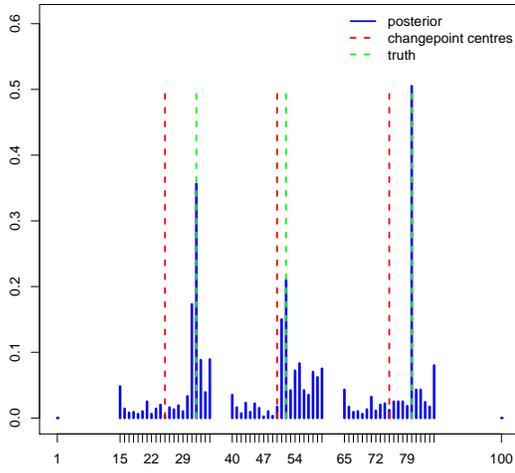
Figure 25: Simulated data ($n_R = 2$). Posterior estimates of the partition of the areal units for each simulation scenario and regime. The estimates are obtained by minimising the Variation of Information loss function.



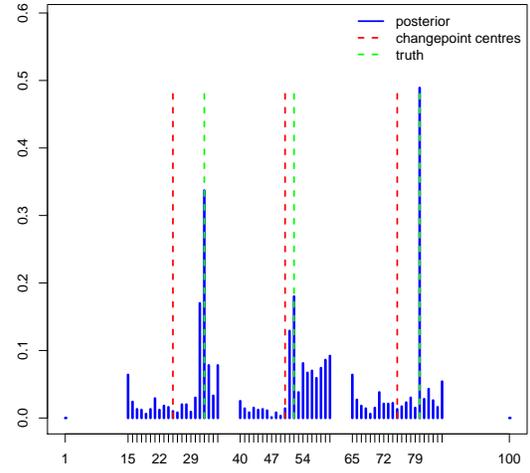
(a) $(n_\lambda, \sigma_{\epsilon_r}^2) = (5, 0.1)$



(b) $(n_\lambda, \sigma_{\epsilon_r}^2) = (5, 1)$



(c) $(n_\lambda, \sigma_{\epsilon_r}^2) = (10, 0.1)$



(d) $(n_\lambda, \sigma_{\epsilon_r}^2) = (10, 1)$

Figure 26: Simulated data ($n_R = 2$). Posterior estimates of the partition of the areal units for each simulation scenario and regime. The estimates are obtained by minimising the Variation of Information loss function.

APPENDIX C: Comparison with competitor models

We report in this Appendix a performance comparison between the proposed model and some of its variations as well as competitors available in the literature. The latter are the RS-aPPM model equipped with either a Dirichlet Process (DP) prior for the partition or the same prior used in Hegarty and Barry [2008] (HB), and the spatio-temporal conditionally auto-regressive models of [Lee et al., 2015] which are available for implementation through the R package `CARBayesST`. In particular, for the latter we focus on the `ST.CARar` model. Based on the previous considerations, when comparing variants of our proposed model, we select the values $(\xi, \kappa) = (2, 1)$. We then specify six different models, namely:

1. RS-aPPM (full)
2. RS-aPPM, DP version ($\xi = 0$)
3. RS-aPPM, parametric version (one cluster)
4. RS-aPPM, HB version: setting $\kappa = 1$ and dropping the $\Gamma(n_j^r)$ terms in (14)
5. ST.CARar ($\rho = 0$)
6. ST.CARar ($\rho = 0.95$)

All the models are evaluated on the same dataset as in Section 4. Simulations for the all six models are run for a total of 50,000 iterations after 100 iterations used as burn-in for the adaptive part of the MCMC algorithm. Thus, the last 5,000 iterations are thinned every second one to retain a sample of size 2,500. We report in Table 3 the posterior mode of the number of clusters within each regime, the LPML and the WAIC for each scenario. The posterior mode of the number of clusters is absent for the parametric and STCARar models, due to the lack of a prior over the partition of the areal units. In general, we can observe a coarser partition of the areal units yielded by the proposed model when compared to the cases corresponding to its DP-only or its HB-only versions, with exception of the second

Table 3: Comparison between different modeling options. Each row corresponds to a different measure, i.e. the posterior mode of the number of clusters, the LPML and the WAIC. Within each sub-square of the table, values are reported for regimes 1/2 (top row) and 3/4 (bottom row).

	RS-aPPM		RS-aPPM DP		Param.	RS-aPPM HB		ST.CARar $\rho = 0$		ST.CARar $\rho = 0.95$		
$\text{mode}(K_I \mathbf{y})$	14	28	14	14	–	–	16	15	–	–	–	–
	11	13	22	17	–	–	18	13	–	–	–	–
LPML (per 10^3)	85.75		-494.95		-487.28	-558.32		-304.55		226.48		
WAIC (per 10^3)	-190.08		3076.18		955.55	4505.62		609.10		-638.13		

regime (weekday night-time). In terms of goodness of fit, the proposed model outperforms competitors, by yielding the highest LPML and lowest WAIC values, with exception of the StCARar model with $\rho = 0.95$. It is interesting to observe that the StCARar model detects the presence of spatial correlation, as reflected by comparing the cases $\rho = 0$ and $\rho = 0.95$. Note that the StCARar models do not allow for any clustering structure estimation, neither do they provide modeling of regimes. It is also worth noting that the StCARar model includes a more sophisticated specification of spatio-temporal random effects than our CAR structure, which may explain the LPML and WAIC values here reported.

APPENDIX D: FURTHER PLOTS

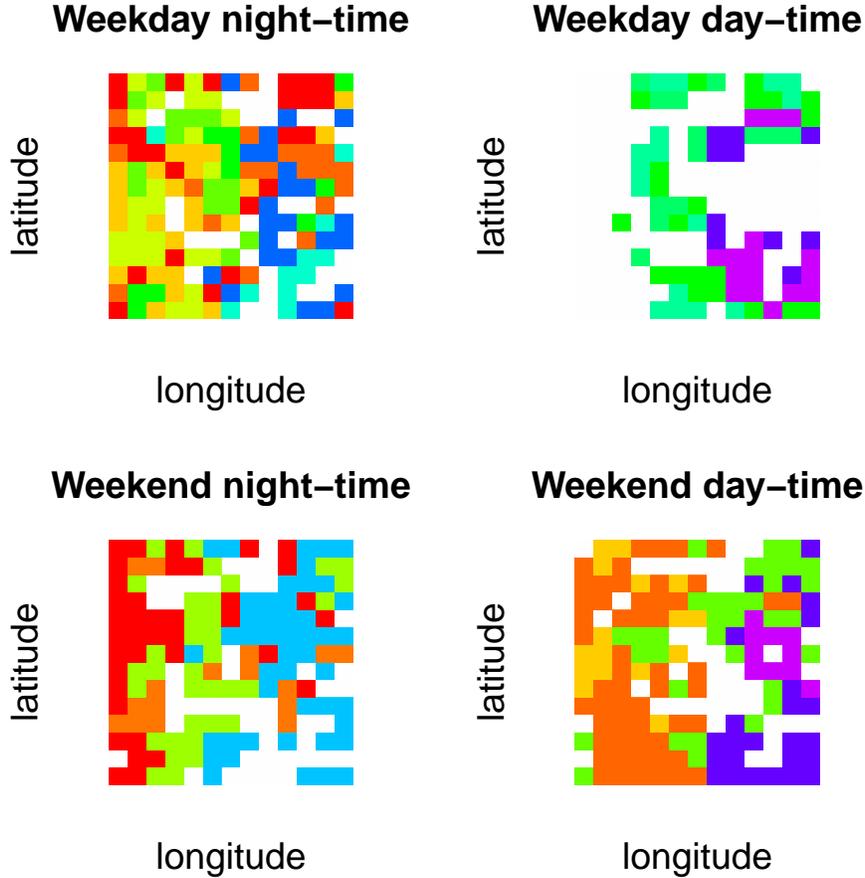


Figure 27: Telecom data. Posterior estimate of the random partition ρ_r , for $r = 1, \dots, n_R = 4$, given by minimizing the VI loss function; hyperparameters in the random partitions prior are equal to $\xi = 1, \kappa = 1$.

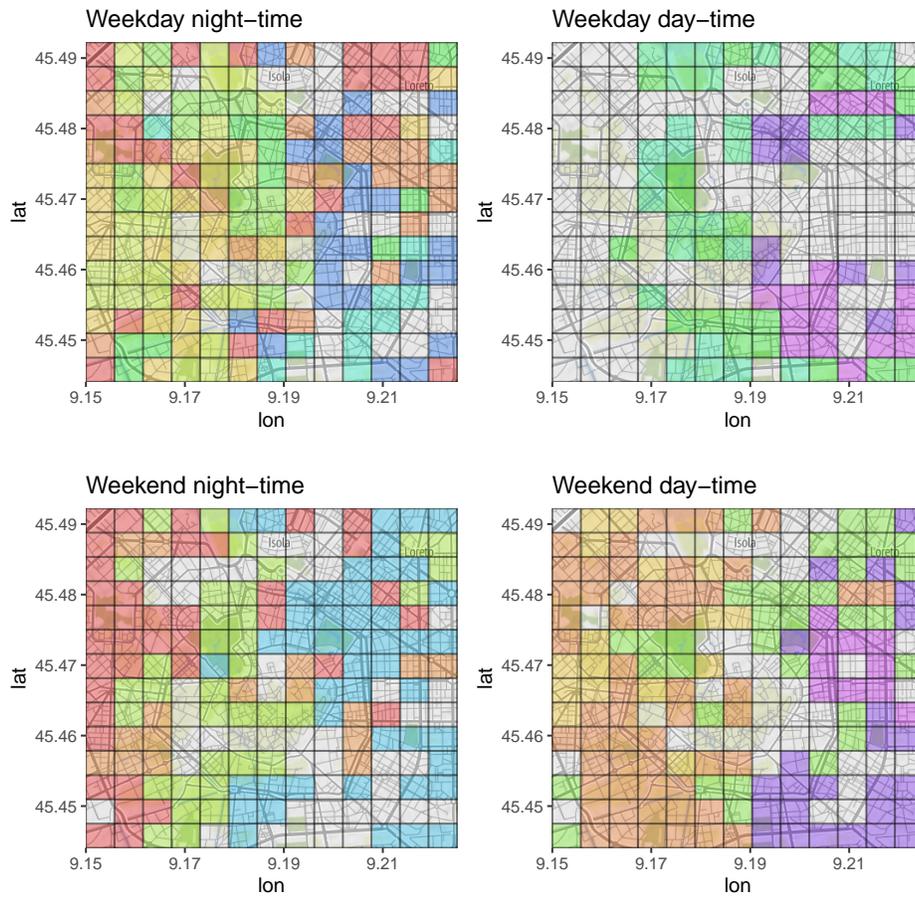


Figure 28: Telecom data. Posterior estimate of the random partition ρ_r , for $r = 1, \dots, n_R = 4$, given by minimizing the VI's loss function; hyperparameters in the random partitions prior are equal to $\xi = 1, \kappa = 1$. A map of the total area is superimposed.

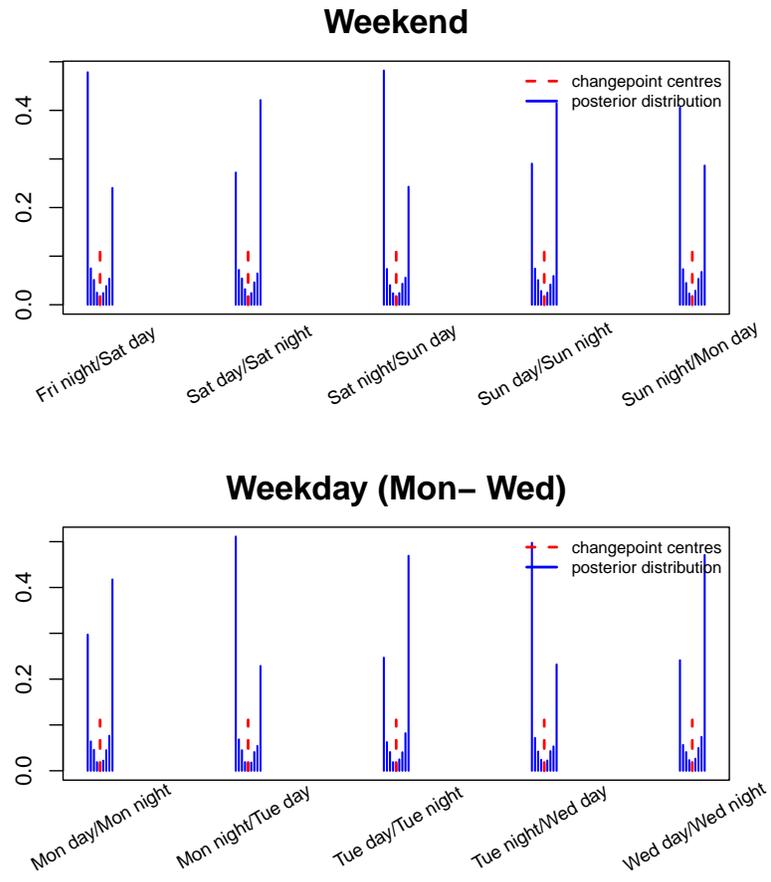


Figure 29: Posterior distribution of the changepoints corresponding to the first weekend and second weekday (Monday to Wednesday) of observations. These are obtained by running the full proposed model with hyperparameters in the random partitions prior equal to $\xi = 2, \kappa = 1$. A map of the total area is superimposed.